

Intrinsic galaxy alignment from angular dependent primordial non-Gaussianity

Kazuhiro Kogai,^a Takahiko Matsubara,^b Atsushi J. Nishizawa,^{a,c}
and Yuko Urakawa^{a,c,d}

^aDepartment of Physics and Astrophysics, Nagoya University,
Chikusa, Nagoya 464-8602, Japan

^bInstitute of Particle and Nuclear Studies,
High Energy Accelerator Research Organization (KEK),
Oho 1-1, Tsukuba 305-0801, Japan

^cInstitute for Advanced Research, Nagoya University,
Chikusa, Nagoya 464-8602, Japan

^dInstitut de Ciències del Cosmos, Universitat de Barcelona,
Martí i Franques 1 08028, Barcelona, Spain

E-mail: kogai@nagoya-u.jp, tmats@post.kek.jp,
atsushi.nishizawa@iar.nagoya-u.ac.jp, urakawa.yuko@h.mbox.nagoya-u.ac.jp

Abstract. In this paper, we explore a detectable imprint of massive fields with integer spins $s \geq 2$, which may be predicted from string theory. It was shown that such a massive non-zero spin field can generate the squeezed primordial bispectrum which depends on the angle between the two wavenumbers. We show that considering the contribution from the massive spin-2 field, the angular dependent primordial non-Gaussianity (PNG) yields a strong scale dependence in the bias parameter for the galaxy alignment, which becomes prominent at small scales. As another example of an angular dependent PNG, we also consider the primordial bispectrum where the angular dependence was introduced by a vector field, while breaking the global rotational symmetry. As a consequence, we find that the B-mode cosmic shear and non-diagonal components do not vanish. These aspects provide qualitative differences from the PNG sourced by massive non-zero spin fields.

Keywords: Primordial non-Gaussianity, Scale dependent bias, Intrinsic galaxy alignment

ArXiv ePrint: [1804.06284](https://arxiv.org/abs/1804.06284)

Contents

1	Introduction	1
2	Preliminaries	3
2.1	Various primordial non-Gaussianities	3
2.1.1	Primordial non-Gaussianity from massive fields	4
2.1.2	Primordial non-Gaussianity with global anisotropy	6
2.2	Bias model	6
2.3	Projection and Decomposition into E/B-mode	7
3	Angular dependent PNG with global isotropy	8
3.1	Angular power spectrum	8
3.2	Numerical analysis	10
3.3	Fisher matrix analysis	13
4	Intrinsic alignment with global anisotropy	16
4.1	Angular dependent PNG with global anisotropy	17
4.2	Angular power spectrum	18
5	Conclusion	21
A	Derivation of scale dependent bias	22
A.1	Galaxy shape	22
A.2	Number density	24
B	Derivation and Feature of Angular power spectra	25
B.1	Calculation of intrinsic galaxy shape with global anisotropy	25
B.2	Rotation of axis	26

1 Introduction

Exploring the physics which governs the very early universe may provide a unique probe of the high energy fundamental theory such as string theory. Especially, the primordial non-Gaussianity (PNG), generated during inflation, encodes the information about non-linear dynamics of the inflationary universe. Given that the inflaton, which played the main role in the inflationary universe by driving the accelerated expansion, had interacted with other fields, the fluctuation of the inflaton can capture the information of these other species.

Especially when the characteristic scale of string theory is not too far from the energy scale of inflation, there may be copious stringy corrections, including contributions of massive higher spin fields. In case such higher spin fields had a non-negligible coupling with the inflaton, we may be able to probe a distinctive signal of stringy corrections by detecting the imprints of these fields on the PNG. In Ref. [1], Arkani-Hamed and Maldacena derived the PNG generated from the massive fields with integer spins s and showed the massive fields with $s \neq 0$, can generate the PNG with a characteristic angular dependence (see also Refs. [2, 3] for earlier studies about imprints of massive scalar fields). To be more explicit, a

massive spin- s field yields a contribution which is proportional to $(\mathbf{k}_L \cdot \mathbf{k}_S)^s$ in the bispectrum with $k_L/k_S \ll 1$, where \mathbf{k}_L and \mathbf{k}_S denote the long and short modes of the bispectrum.

The measurements of the Cosmic Microwave Background (CMB) have given the tightest constraints on various types of the PNG, including the angular dependent PNG [4]. A significant improvement of the constraints, however, may come out from next generation large scale structure (LSS) surveys such as *Large Synoptic Survey Telescope* (LSST) [5], *Euclid* [6] and *Wide-Field Infrared Survey Telescope* (WFIRST) [7]. The angular independent local-type bispectrum, parametrized by $f_{\text{NL}}^{\text{loc}}$, generates a strong scale-dependence in the halo bias parameter [8–10], providing a powerful tool to explore the PNG. An extensive review on this subject can be found e.g. in Refs. [11, 12].

More recently, in Ref. [13], Schmidt et al. showed that the angular dependent PNG, which may encode the information on the non-zero spin fields, generates a scale-dependent contribution in the bias parameter for the intrinsic galaxy shape. The intrinsic galaxy alignment has been detected for the early-type galaxies, while for late-type galaxies, it was measured to be null-consistent [14–16] (see also Ref. [17]). The cosmic shear originates from the intrinsic alignment as well as the gravitational lensing. The next generation imaging surveys [5–7] are expected to measure the shape and distance of galaxies with unprecedented precisions. The constraint on the amplitude of the angular dependent PNG obtained in Ref. [13] is looser than the one obtained from the CMB measurements [4]. The dominant limitation of detecting the squeezed PNG from the scale-dependent bias is due to the cosmic variance, because the signal of the PNG in the bias parameter appears at large scales. This limitation can be circumvented by using multi-tracers [18, 19]. In fact, in Ref. [20], by using multi-tracers, a tighter constraint was obtained also for the angular dependent PNG. (In Ref. [21], constraints on various types of the angular independent PNG were obtained by using multi-tracer technique.)

In Refs. [4, 13, 20], the imprints of the massive fields with $s \neq 0$ are investigated by focusing on the angular dependent contributions. In addition, here, we will also focus on the fact that the amplitude of the PNG generated from such massive fields exhibits a characteristic scale dependence, which was not taken into account in Refs. [4, 13, 20]. Since the PNG was generated through an excitation of the massive field, the amplitude shows an oscillatory feature whose frequency is determined by the mass scale M_s (when M_s is in the principal series) [1–3]. In addition, as a consequence of the dilution due to the cosmic expansion, the amplitude of the “squeezed” PNG is suppressed by $(k_L/k_S)^{\frac{3}{2}}$. In this paper, we will show that including the scale-dependent amplitude in accordance with the model prediction leads to a qualitatively different scale dependent bias from the one obtained in Refs. [13, 20]. In particular, we will find that because of the scale dependent coefficient $(k_L/k_S)^{\frac{3}{2}}$, the signal of the PNG becomes more prominent at smaller scales. (A related issue was discussed for another bias parameter in Refs. [22, 23].)

In this paper, we also consider another origin of the intrinsic galaxy alignment. The PNG generated from the massive fields with $s \neq 0$ in a quasi de Sitter spacetime preserves the global rotational symmetry, while it depends on the angle between the two wavenumbers \mathbf{k}_L and \mathbf{k}_S . On the other hand, when there exists a vector field during inflation, it also can generate an angular dependent PNG, breaking the global rotational symmetry [24, 25]. In this case, we will show the spatial distribution of the intrinsic alignment also exhibits the violation of the global isotropy. Meanwhile, a limitation of the survey region can induce a difference between the genuine distribution of the fluctuation prior to observations and the apparent distribution [26, 27]. Because of that, even if the genuine distribution preserves the

global rotational symmetry, the observed distribution can exhibit an apparent violation of the symmetry.

Having these possibilities in mind, we compute the spectra of the cosmic shear and the galaxy overdensity, when the distribution of the intrinsic galaxy shape violates the global rotational symmetry. Comparing the resultant spectra to those obtained by using the PNG generated from the massive spin-2 field, we address whether we can qualitatively distinguish these two different cases or not. Unless this is possible, the signal from a massive spin-2 field such as Kaluza-Klein graviton can degenerate with signals from other sources. We will find that while these two cases predict similar spectra of the galaxy overdensity and the E-mode cosmic shear, the case with the global anisotropy predicts a non-zero B-mode cosmic shear due to the parity violation and a mixing of non-diagonal modes in the spherical harmonic expansion due to the violation of the global rotational symmetry.

This paper is organized as follows. In Sec. 2, we briefly describe the ansatz of the PNGs whose imprints will be addressed in this paper. Then, we summarize the basis formulae we use in computing the angular power spectra. In Sec. 3, following Ref. [13], we compute the angular power spectra of the galaxy overdensity and the cosmic shear when there exists the angular dependent PNG generated from massive non-zero spin fields. Using this result, we also perform the Fisher matrix analysis to estimate the forecast on uncertainties of the non-Gaussian parameters. In Sec. 4, we compute the predicted cosmic shear, when the distribution of the intrinsic alignment does not preserve the global rotational symmetry, clarifying the difference from the prediction in Sec. 3. In Sec. 5, we summarize our results and discuss remaining issues. A detailed computation of the formulae in Sec. 5 is summarized in Appendix A and Appendix B.

In this paper, we assume the Planck fiducial [28] flat Λ CDM cosmology with $\Omega_{\text{b}0}h^2 = 0.022$, $\Omega_{\text{CDM}0}h^2 = 0.12$, $h = 0.67$, $n_s = 0.9645$, $k_p = 0.05 \text{ Mpc}^{-1}$. With $\Omega_{\text{b}0}$ and $\Omega_{\text{CDM}0}$, $\Omega_{\text{m}0}$ is defined as $\Omega_{\text{m}0} \equiv \Omega_{\text{b}0} + \Omega_{\text{CDM}0}$. To calculate the matter power spectra at present and the transfer function, we use the public code CAMB [29].

2 Preliminaries

In this section, we summarize the ansatz of the PNGs which we consider in this paper. Then, we briefly describe basic formulae which will be used in our computation. A more detailed explanation can be found, e.g., in Refs. [13, 30].

2.1 Various primordial non-Gaussianities

Weak gravitational lensing stretches an image of cosmological structures. We can probe the projected distribution of gravitational potential lying between source galaxies and us by measuring shapes of galaxies. However, this cosmic shear signal can be contaminated by a local coherence of intrinsic shapes of source galaxies. In Ref. [31], Catalan et al. discussed several cases where a position-dependent gravitational force, characterized by the tidal force, leads to an intrinsic distortion of galaxies. In Ref. [32], it was argued that the cross-correlation between the intrinsic shear and the gravitational lensing shear can lead to a non-negligible signal. Extensive reviews on the intrinsic galaxy alignment can be found e.g., in Refs. [33, 34].

The intrinsic shear of galaxies yields a noise contamination in extracting the information of the gravitational lensing shear out of detected cosmic shear signals. However, as was pointed out in Ref. [13], the intrinsic galaxy alignment itself provides information on the squeezed PNG which depends on the angle between two momenta \mathbf{k}_L and \mathbf{k}_S . In this paper,

we further explore this possibility, considering a wider class of PNGs which can generate the intrinsic shape correlation. In this subsection, we summarize the ansatz of the PNGs we address in this paper.

2.1.1 Primordial non-Gaussianity from massive fields

A well-controlled model of inflation from string theory possesses the energy scale hierarchy as $H (< M_{\text{KK}}) < M_{\text{string}} < M_{\text{pl}}$, where H , M_{KK} , and M_{string} denote the Hubble parameter during inflation, the Kaluza-Klein scales, and the string scale, respectively (see, e.g., Ref. [35]), i.e., there is a hierarchical energy gap between H and M_{string} . On the other hand, when H is not very far from M_{string} , there will be copious stringy corrections, which may include those of massive spin fields with their spins $s \geq 2$. If such massive non-zero spin fields had interacted with the inflaton during inflation, it may be possible to explore an imprint of the stringy corrections by measuring the primordial curvature perturbation ζ , while building such a model remains still rather challenging.

In Ref. [1], making full use of the de Sitter symmetry, Arkani-Hamed and Maldacena derived the squeezed bispectrum of ζ which was generated through an interaction between the inflaton and a massive higher spin field with spin s and mass M_s in the principal series, i.e.,

$$\frac{M_0}{H} \geq \frac{3}{2}, \quad \frac{M_s}{H} \geq s - \frac{1}{2} \quad (s \neq 0), \quad (2.1)$$

as

$$B^{\text{massive}}(\mathbf{k}_L, \mathbf{k}_S) \simeq \sum_{s=0, 2, \dots} A_s^{(\zeta)} \mathcal{P}_s(\hat{\mathbf{k}}_L \cdot \hat{\mathbf{k}}_S) \left(\frac{k_L}{k_S}\right)^{\frac{3}{2}} \times \cos(\nu_s \ln(k_L/k_S) + \varphi_s) P(k_L) P(k_S), \quad (2.2)$$

with $k_L/k_S \ll 1$ and $\hat{\mathbf{k}}_\alpha \equiv \mathbf{k}_\alpha/k_\alpha$ ($\alpha = L, S$). Here, \mathcal{P}_s denotes the Legendre polynomials, given by

$$\mathcal{P}_0(x) = 1, \quad \mathcal{P}_1(x) = x, \quad \mathcal{P}_2(x) = \frac{1}{2}(3x^2 - 1), \dots, \quad (2.3)$$

and $P(k)$ denotes the power spectrum of ζ .

Since this bispectrum describes a non-local contribution generated through an interaction between the inflaton and the massive field, it includes non-analytic terms with non-integer powers of momenta. The parameter ν_s , which determines the frequency of the oscillation, is given by the imaginary part of the scaling dimension for each field¹. For a massive scalar field with mass M_0 , ν_0 is given by

$$\nu_0 = \sqrt{\left(\frac{M_0}{H}\right)^2 - \frac{9}{4}} \quad (2.5)$$

¹The scaling dimension of a spin- s massive field in $(d+1)$ -dimensional de Sitter space is given by [36]

$$\Delta_s = \frac{d}{2} \pm \sqrt{\left(s + \frac{d-4}{2}\right)^2 - \frac{M_s^2}{H^2}}. \quad (2.4)$$

and for a massive spin- s field with mass M_s , ν_s is given by

$$\nu_s = \sqrt{\left(\frac{M_s}{H}\right)^2 - \left(s - \frac{1}{2}\right)^2}. \quad (2.6)$$

The suppression factor $(k_L/k_S)^{3/2}$ appears, since the massive field was diluted at least until the Hubble crossing of the short mode k_S . In Ref. [37], it was shown that when the propagation speed of the inflaton is smaller than 1, the Hubble crossing is shifted to an earlier time, relaxing the suppression due to the dilution. Alternatively, this suppression factor may be overcome by considering interactions. Notice that in Eq. (2.2), the contributions from odd spin fields vanish because of the symmetry of the de Sitter spacetime [1]. Meanwhile, a deviation from the de Sitter spacetime can enhance the contributions from odd spin fields. The amplitude of the bispectrum $A_s^{(\zeta)}$ is typically suppressed by two ways in slow-roll inflation models: suppressions by slow-roll parameters, which appear from interaction vertices, and also by the factor $e^{-\pi\nu_s}$, whose square give the Boltzmann factor of a massive field. (About an expression of the phase φ_s , see e.g., Ref. [37].)

The bispectrum (2.2) was originally evaluated at the time when all the modes exit into the super Hubble scales [1]. Notice that to connect the bispectrum evaluated at the Hubble crossing time with observable fluctuations, we need to solve the succeeding time evolution. In Refs. [38, 39], considering a rather general setup, which can also apply to an inflation model with massive non-zero spin fields, the condition that ensures the time conservation of ζ in super Hubble scales was derived by generalizing the Weinberg's adiabatic condition [40]. In the following, we assume that the adiabatic condition is satisfied and the curvature perturbation ζ is conserved all along in the super Hubble regime². Changing the variable from ζ to the primordial Bardeen potential ϕ as $\phi = (3/5)\zeta$, we consider the squeezed bispectrum for ϕ given by

$$B_\phi(\mathbf{k}_L, \mathbf{k}_S) \simeq \sum_{s=0,2,\dots} A_s \mathcal{P}_s(\hat{\mathbf{k}}_L \cdot \hat{\mathbf{k}}_S) \left(\frac{k_L}{k_S}\right)^{\tilde{\Delta}_s} \times \cos(\nu_s \ln(k_L/k_S) + \varphi_s) P_\phi(k_L) P_\phi(k_S), \quad (2.7)$$

where $A_s \equiv (5/3)A_s^{(\zeta)}$ and P_ϕ denotes the power spectrum of ϕ . In Eq. (2.2), $\tilde{\Delta}_s$ is given by $3/2$. When we set $\tilde{\Delta}_0 = 0$ and $\nu_0 = 0$, the term with A_0 gives the squeezed bispectrum parametrized by $f_{\text{NL}}^{\text{loc}} = A_0 \cos \varphi_0/4$.

In Ref. [13], considering the bispectrum (2.7) with the scaling dimension Δ_s set to 0, which does not include the dilution factor nor the oscillatory contribution, it was shown that the angular dependent PNG from a massive spin-2 field leads to an intrinsic galaxy alignment at large scales. As is expected, by including the factor $(k_L/k_S)^{3/2}$, the signal of the PNG at large scales becomes less significant. Nevertheless, we will find that in such case, the signal of the PNG given by (2.7) can become prominent at smaller scales. This is common for massive particles in the principal series with general integer spins.

In the following, taking into account more general cases, e.g., where the suppression due to the dilution is relaxed by considering interactions or a deviation of the propagation speed from 1, or where the massive field is in the complementary mass range, we also consider the case where $\tilde{\Delta}_s$ and ν_s are not given by $\tilde{\Delta}_s = 3/2$ and Eqs. (2.5)-(2.6).

²In solid inflation [41], it was shown that a similar angular dependent PNG to those from higher spin fields can be generated. Notice, however, that there are several qualitative differences in these two cases such as the non-conservation of the curvature perturbation at large scales in the former case.

2.1.2 Primordial non-Gaussianity with global anisotropy

Detecting an imprint of the PNG (2.2) provides a distinctive signal of higher spin fields which may be predicted by string theory. In order to assert that the enhanced intrinsic alignment [13] is a unique signal of such spinning fields, the signal has to be distinguishable from those generated by other sources. As an example, let us consider a PNG given by

$$\bar{B}_\phi(\mathbf{k}_L, \mathbf{k}_S; \hat{\mathbf{p}}) = \sum_{l=0}^{\infty} \left[\bar{A}_l + \bar{B}_l \hat{\mathbf{k}}_L \cdot \hat{\mathbf{k}}_S + \dots \right] i^{\frac{1-(-1)^l}{2}} \mathcal{P}_l(\hat{\mathbf{p}} \cdot \hat{\mathbf{k}}_S) P_\phi(k_L) P_\phi(k_S), \quad (2.8)$$

where l sums over all non-negative integers. In addition to the terms which depend on the angle between \mathbf{k}_L and \mathbf{k}_S , the bispectrum \bar{B}_ϕ also contains the terms which depend on the constant unit vector $\hat{\mathbf{p}}$. While the global rotational symmetry is preserved for the bispectrum B_ϕ , it is not the case for \bar{B}_ϕ . In the square brackets, we abbreviated terms with more powers of $\hat{\mathbf{k}}_L \cdot \hat{\mathbf{k}}_S$. The coefficients \bar{A}_l and \bar{B}_l do not depend on $\hat{\mathbf{k}}_S$, but can depend on k_L , k_S , and $\hat{\mathbf{k}}_L \cdot \hat{\mathbf{p}}$.

The PNG (2.8), which depends on the constant vector can be generated, when the primordial curvature perturbation is also sourced by a vector field (see e.g., Refs. [24, 25]). Even if the contribution from the vector field, which breaks the global rotational symmetry, is suppressed in the power spectrum, being compatible with the current CMB observations [42, 43], it is not necessarily suppressed also in the higher-point functions. (The global anisotropy in the galaxy and CMB spectra was studied e.g., in Refs. [44–46].) This possibility was explored in Ref. [24] and claimed that this is in fact possible in the presence of an enhanced cubic interaction. (See also Refs. [47, 48].)

Similarly to the case with the angular dependent PNG with the global isotropy (2.2), the angular dependent PNG without the global isotropy (2.8) also can deform intrinsic shapes of galaxies. Having said this, let us ask the following question; Given that these two different cases are not distinguishable from the power spectrum but the difference shows up only from non-Gaussian correlators such as the bispectrum, can we observationally distinguish these two cases? If this is not possible, the enhanced cosmic shear due to the intrinsic alignment cannot be a unique signal which shows the presence of massive fields with the spin $s \geq 2$ in the early universe. We will address this question in the succeeding sections.

2.2 Bias model

In this paper, following Ref. [13] (see also Ref. [49]), we assume a local expansion of the galaxy number density perturbation δ_n and the three-dimensional galaxy shape function, defined as

$$g_{ij} \equiv [\text{Tr } I_{kl}]^{-1} \left(I_{ij} - \frac{1}{3} \delta_{ij} \text{Tr } I_{kl} \right), \quad (2.9)$$

with the second moment of the surface brightness of galaxies I_{ij} as follows

$$\delta_n(\mathbf{x}, z) = b_1^n(z) \delta(\mathbf{x}, z) + \frac{1}{2} b_2^n(z) \delta^2(\mathbf{x}, z) + \frac{1}{2} b_t^n(z) (K_{ij})^2(\mathbf{x}, z) + \dots, \quad (2.10)$$

$$g_{ij}(\mathbf{x}, z) = b_1^I(z) K_{ij}(\mathbf{x}, z) + \frac{1}{2} b_2^I(z) K_{ij}(\mathbf{x}, z) \delta(\mathbf{x}, z) + \frac{1}{2} b_t^I(z) \left[K_{ik} K_j^k - \frac{1}{3} \delta_{ij} (K_{lm})^2 \right] (\mathbf{x}, z) + \dots \quad (2.11)$$

at each redshift z and each position \mathbf{x} . Here, δ denotes the perturbation of the dark matter energy density and K_{ij} denotes the tidal tensor, defined as

$$K_{ij} = \frac{1}{4\pi G \bar{\rho} a^2} \left[\partial_i \partial_j - \frac{1}{3} \delta_{ij} \nabla^2 \right] \Phi = \mathcal{D}_{ij} \delta, \quad (2.12)$$

where $\mathcal{D}_{ij} \equiv \partial^i \partial^j / \partial^2 - \delta_{ij} / 3$. Here we introduced the bias parameters $b_i^n(z)$ and $b_i^l(z)$ with $i = 1, 2, \dots$, $b_t^n(z)$, and $b_t^l(z)$. In Eq. (2.11), we assume that the galaxies are deformed only by the tidal force.

In actual measurements of the cosmic shear, we observe the intrinsic shapes of galaxies which are projected onto the two dimensional sphere (in addition to the lensing effect):

$$\gamma_{1ij} \equiv \left(\mathcal{P}_i^k \mathcal{P}_j^l - \frac{1}{2} \mathcal{P}_{ij} \mathcal{P}^{kl} \right) g_{kl}, \quad (2.13)$$

where \mathcal{P}_{ij} is the projection tensor defined as

$$\mathcal{P}_{ij} \equiv \delta_{ij} - \hat{n}_i \hat{n}_j, \quad (2.14)$$

by using the unit vector along the line of sight $\hat{\mathbf{n}}$.

2.3 Projection and Decomposition into E/B-mode

Next, we decompose the traceless 2-tensor projected on the two-dimensional sky γ_{ij} into the two components which transform as a spin $s = \pm 2$ field. Deferring a detailed computation e.g. to Ref. [30], here we just summarize our notation. We express the orthonormal coordinate system defined for the normal vector along the line-of-sight direction $\hat{\mathbf{n}}$ as $(\mathbf{e}_\psi, \mathbf{e}_\theta, \hat{\mathbf{n}})$, where \mathbf{e}_θ and \mathbf{e}_ψ denote the two bases for the azimuthal and colatitude angles. Using \mathbf{e}_θ and \mathbf{e}_ψ , we introduce

$$\mathbf{m}_\pm \equiv \frac{1}{\sqrt{2}} (\mathbf{e}_\theta \mp i \mathbf{e}_\psi) = \frac{1}{\sqrt{2}} \begin{pmatrix} \cos \theta \cos \psi \pm i \sin \psi \\ \cos \theta \sin \psi \mp i \cos \psi \\ -\sin \theta \end{pmatrix}, \quad (2.15)$$

which satisfy

$$m_\pm^i m_{\pm i} = 0, \quad m_\pm^i m_{\mp i} = 1, \quad m_\pm^i \hat{n}_i = 0, \quad \mathcal{P}_i^j m_{\pm j} = m_{\pm i}. \quad (2.16)$$

Under a rotation around $\hat{\mathbf{n}}$ by an angle ψ , \mathbf{m}_\pm transform as spin ± 1 vectors, i.e., $\mathbf{m}_\pm \rightarrow e^{\pm i\psi} \mathbf{m}_\pm$.

Using \mathbf{m}_\pm , we define spin ± 2 functions

$${}_{\pm 2}\gamma \equiv m_\mp^i m_\mp^j \gamma_{ij}, \quad (2.17)$$

with which we can expand γ^{ij} as $\gamma^{ij} = {}_{+2}\gamma m_+^i m_+^j + {}_{-2}\gamma m_-^i m_-^j$. Using the coefficient of the expansion in terms of the spin weighted spherical harmonics ${}_{\pm 2}Y_{lm}$, given by

$$a_{lm} = \int d\Omega {}_{\pm 2}\gamma(\mathbf{n}) [{}_{\pm 2}Y_{lm}(\hat{\mathbf{n}})]^* = \sqrt{\frac{(l-2)!}{(l+2)!}} \int d\Omega \bar{\delta}^2 {}_{+2}\gamma(\hat{\mathbf{n}}) Y_{lm}^*(\hat{\mathbf{n}}), \quad (2.18)$$

we define the E-mode and the B-mode as ³

$$a_{lm}^{\text{E}} \equiv \frac{1}{2} \left[a_{lm} + (-1)^{|m|} a_{l-m}^* \right], \quad (2.19)$$

$$a_{lm}^{\text{B}} \equiv \frac{1}{2i} \left[a_{lm} - (-1)^{|m|} a_{l-m}^* \right]. \quad (2.20)$$

Here, $\bar{\delta}$ denotes spin-lowering operators, given by [30]

$$\bar{\delta}_s f = -\sin^s \theta \left[\partial_\theta + \frac{i}{\sin \theta} \partial_\phi \right] (\sin^{-s} \theta_s f). \quad (2.21)$$

Under the parity transformation, the E-mode and the B-mode transform as $a_{lm}^{\text{E}} \rightarrow (-1)^l a_{lm}^{\text{E}}$ and $a_{lm}^{\text{B}} \rightarrow (-1)^{l+1} a_{lm}^{\text{B}}$, respectively. Meanwhile, δ_n can be expanded by the spherical harmonics Y_{lm} and we express the coefficient as a_{lm}^n . When the global isotropy is preserved, the angular power spectra are given in the form

$$\langle a_{lm}^X a_{l'm'}^{Y*} \rangle = C_l^{XY} \delta_{l,l'} \delta_{m,m'}, \quad (2.22)$$

with $X, Y = \text{n, E, B}$, which denote the perturbations of the galaxy number density, the E-mode, and the B-mode, respectively.

3 Angular dependent PNG with global isotropy

In this section, we compute the influence of the PNG described in the previous section on the power spectra for $X = \text{n, E, and B}$.

3.1 Angular power spectrum

The presence of a PNG modifies the relation between the galaxy distribution and the distribution of the gravitational potential. As was argued in Ref. [13], when we assume the local expansion for δ_n as in Eq. (2.10), only the angular independent PNG, i.e., the term which is proportional to \mathcal{P}_0 in Eq. (2.7), contributes to the scale-dependent bias between δ and δ_n (for a more general expansion of δ_n , see Ref. [50]). Similarly, with Eq. (2.11), only the angular dependent PNG which is proportional to \mathcal{P}_2 contributes to the scale-dependent bias of g_{ij} . In fact, when the primordial bispectrum is given by Eq. (2.7), as is well known, the squeezed non-Gaussianity generates the strong scale dependence in the effective bias parameter [8],

$$\delta_n(z, \hat{\mathbf{n}}) = \int \frac{d^3 \mathbf{k}}{(2\pi)^{\frac{3}{2}}} e^{ix\hat{\mathbf{k}} \cdot \hat{\mathbf{n}}} b_{\text{eff}}^{\text{n}}(z, k) \delta(z, \mathbf{k}), \quad (3.1)$$

and

$$\pm 2\gamma_{\text{I}}(z, \hat{\mathbf{n}}) = \int \frac{d^3 \mathbf{k}}{(2\pi)^{\frac{3}{2}}} e^{ix\hat{\mathbf{k}} \cdot \hat{\mathbf{n}}} \hat{k}_\pm^2 b_{\text{eff}}^{\text{I}}(z, k) \delta(z, \mathbf{k}), \quad (3.2)$$

where the scale dependent bias parameters are given by

$$b_{\text{eff}}^{\text{n}}(z, k) \equiv b_1^{\text{n}} + \frac{b_{\text{NG}}^{\text{n}} A_0}{2} \left(\frac{k}{k_*} \right)^{\bar{\Delta}_0} \mathcal{M}^{-1}(z, k) \cos \left(\nu_0 \ln \left(\frac{k}{k_*} \right) + \Theta_0 \right) \quad (3.3)$$

³Since we use the spherical harmonics whose complex conjugate is given by $Y_{lm}^* = (-1)^{|m|} Y_{l-m}$, we need to insert $(-1)^{|m|}$ in the definitions of a_{lm}^{E} and a_{lm}^{B} .

for the perturbation of the number density and

$$b_{\text{eff}}^{\text{I}}(z, k) \equiv b_1^{\text{I}} + 3b_{\text{NG}}^{\text{I}}A_2 \left(\frac{k}{k_*}\right)^{\tilde{\Delta}_2} \mathcal{M}^{-1}(z, k) \cos\left(\nu_2 \ln\left(\frac{k}{k_*}\right) + \Theta_2\right) \quad (3.4)$$

for the intrinsic alignment. Here, using φ_s , the phase included in the PNG, the phase Θ_s can be determined for a given halo model. $\mathcal{M}(k, z)$ relates ϕ and δ as $\delta(z, \mathbf{k}) = \mathcal{M}(z, k)\phi(\mathbf{k})$ and is given by

$$\mathcal{M}(z, k) \equiv \frac{2}{3} \frac{k^2 T(k) D(z)}{\Omega_{\text{m}0} H_0^2}, \quad (3.5)$$

where $T(k)$ is the transfer function and $D(z)$ is the growth factor. A computation for $\tilde{\Delta}_0 = \tilde{\Delta}_2 = 0$ and $\nu_0 = \nu_2 = 0$ is given in Ref. [13]. An extension to include non-zero values of $\tilde{\Delta}_0$, $\tilde{\Delta}_2$, ν_0 , and ν_2 proceeds straightforwardly. For $\nu_0 \neq 0$ or/and $\nu_2 \neq 0$, the oscillation in the PNG leads to the oscillatory feature in the effective bias parameters $b_{\text{eff}}^{\text{I}}$ and $b_{\text{eff}}^{\text{n}}$.

The non-linear bias parameters b_{NG}^{n} and b_{NG}^{I} appeared after renormalizing the divergent contributions [13]. Here, k_* is a reference scale, which appears as the lower end of the integral over k_{S} in our computation. To be consistent with the squeezed configuration of the PNG, the wavenumber \mathbf{k} for which we study the imprint should satisfy $k < k_*$. In the following, we set k_* as $k_* = 1[\text{Mpc}^{-1}]$, which gives a typical mass of a galactic halo ⁴.

The intrinsic alignment itself is not directly observable. The cosmic shear that we observe is a summation of the intrinsic alignment and the gravitational lensing shear. Using Eqs. (3.1) and (3.2) and including the lensing effect, we obtain

$$C_l^{\text{EE}} = \frac{2}{\pi} \frac{(l-2)!}{(l+2)!} \int k^2 dk P_{\text{m}}(k) [F_l^{\text{I}}(k) + F_l^{\text{G}}(k)]^2, \quad (3.6)$$

$$C_l^{\text{nE}} = \frac{2}{\pi} \sqrt{\frac{(l-2)!}{(l+2)!}} \int k^2 dk P_{\text{m}}(k) [F_l^{\text{I}}(k) + F_l^{\text{G}}(k)] F_l^{\text{n}}(k), \quad (3.7)$$

$$C_l^{\text{nn}} = \frac{2}{\pi} \int k^2 dk P_{\text{m}}(k) [F_l^{\text{n}}(k)]^2, \quad (3.8)$$

with

$$F_l^{\text{I}}(k) = \frac{1}{2} \frac{(l+2)!}{(l-2)!} \int dz \frac{dN_{\text{I}}}{dz} \frac{D(z)}{D(0)} \frac{j_l(x)}{x^2} b_{\text{eff}}^{\text{I}}(z, k), \quad (3.9)$$

$$F_l^{\text{n}}(k) = \int dz \frac{dN_{\text{n}}}{dz} \frac{D(z)}{D(0)} j_l(x) b_{\text{eff}}^{\text{n}}(z, k), \quad (3.10)$$

$$F_l^{\text{G}}(k) = \frac{1}{2} \frac{(l+2)!}{(l-2)!} \int_0^{\chi_{\text{max}}} \frac{d\chi}{\chi} \frac{3H_0^2 \Omega_{\text{m}0}}{k^2} \frac{(1+z)D(z(\chi))}{D(0)} j_l(x) \int_{\chi}^{\chi_{\text{max}}} d\tilde{\chi} H(\tilde{\chi}) \frac{dN_{\text{G}}}{dz} \frac{(\tilde{\chi} - \chi)}{\tilde{\chi}}, \quad (3.11)$$

where $P_{\text{m}}(k)$ denotes the matter power spectrum evaluated at present, j_l denotes the spherical Bessel function of order l . We put the indices {I, n, G} to denote the intrinsic alignment, the perturbation of the number density, and the gravitational lensing shear, respectively. In this

⁴A change due to a different choice of k_* degenerates with other parameters such as A_0 , $b_{\text{NG}}^{\text{I}}A_2$, Θ_0 , and Θ_2 . In Ref. [22], k_* (in their notation, $R_* = 1/k_*$) is determined by the Lagrangian radius of the halo of interest.

paper, we neglect the non-linear loop corrections. Then, the absence of the parity violation leads to the vanishing B-mode and the global rotational symmetry ensures the absence of a correlation between different multipoles.

To compute the contributions from the fluctuations at a given redshift along the line of sight, in Eqs. (3.9)-(3.11), we introduce the redshift distribution function of galaxies dN_a/dz with $a = \text{I, n and G}$. We assume the functional form for dN_a/dz as

$$\frac{dN_a}{dz} \propto \left(\frac{z}{z_{*a}}\right)^{\alpha_a} \exp\left[-\left(\frac{z}{z_{*a}}\right)^{\beta_a}\right]. \quad (3.12)$$

Following Refs. [5, 51], we choose $\alpha_{\text{I}} = \alpha_{\text{G}} = 1.24$ and $\beta_{\text{I}} = \beta_{\text{G}} = 1.01$, and $\alpha_{\text{n}} = 1.25$, $\beta_{\text{n}} = 1.26$, and $z_{*\text{n}} = 1.0$, considering an LSST like survey. Here, to study how the forecast on parameter uncertainties changes, depending on the galaxy redshift distribution, we leave $z_{*\text{I}}$, which we assume to be equal to $z_{*\text{G}}$, as a free parameter. This parameter amounts to 0.51 for LSST lensing survey. In a more realistic setup, we should choose a different distribution for dN_{I}/dz and dN_{G}/dz , since the intrinsic alignment has been detected only for early-type galaxies [14–16].

3.2 Numerical analysis

Using Eqs. (3.6) - (3.8), in this subsection, we numerically compute the power spectra for the perturbation of the number density and the E-mode cosmic shear. Here, we adopt the Limber approximation [52, 53] for $l \geq 60$. For a simple halo model, the non-linear bias parameter for the number density b_{NG}^{n} is given by [8, 9, 54] (see also Ref. [55])

$$b_{\text{NG}}^{\text{n}} = (b_1^{\text{n}} - 1)\delta_{\text{c}}, \quad (3.13)$$

where $\delta_{\text{c}} (= 1.686)$ denotes the critical density for spherical collapse. Along the line with the convention of the tidal alignment [56], we set the linear bias parameter b_1^{I} as

$$b_1^{\text{I}}(z) = \bar{b}_1^{\text{I}} \Omega_{\text{m}0} \frac{D(0)}{D(z)}, \quad (3.14)$$

which is consistent with observations of luminous red galaxies. Meanwhile, the non-linear bias parameter for the galaxy shape b_{NG}^{I} is not very well known. In this paper, assuming that b_{NG}^{I} is a constant parameter which is comparable to b_1^{I} [13], we parametrize b_{NG}^{I} as

$$b_{\text{NG}}^{\text{I}} = \bar{b}_{\text{NG}}^{\text{I}} \bar{b}_1^{\text{I}} \Omega_{\text{m}0} = \bar{b}_{\text{NG}}^{\text{I}} b_1^{\text{I}}(z) \frac{D(z)}{D(0)}. \quad (3.15)$$

Here, $\bar{b}_{\text{NG}}^{\text{I}}$ is another constant parameter.

The left panel of Fig. 1 shows the angular spectrum of the E-mode cosmic shear, given in Eq. (3.6) for three different initial conditions (at the reheating surface). The blue line shows the case with $A_2 = 0$, which includes the case with the Gaussian initial condition. The green dotted line shows the case with $\bar{b}_{\text{NG}}^{\text{I}} A_2 = 100$ and $\tilde{\Delta}_2 = \nu_2 = \Theta_2 = 0$, which was studied in Ref. [13]. The red dashed line shows the case with $\bar{b}_{\text{NG}}^{\text{I}} A_2 = 8000$, $\tilde{\Delta}_2 = 3/2$, $\nu_2 = 3$, and $\Theta_2 = 0$, which can be generated from the massive spin 2 field. Here, we set the (remaining) bias parameters as $b_1^{\text{n}} = 2$, $\bar{b}_1^{\text{I}} = -0.1$, and $\bar{b}_{\text{NG}}^{\text{I}} = 1$ [13] and z_{*a} with $a = \text{I, G}$ as $z_{*\text{I}} = z_{*\text{G}} = 0.3$. As was already argued, other terms in the ansatz of the PNG (2.2) do not contribute to the cosmic shear for the bias ansatz assumed here (see Sec. 2.2). The right panel

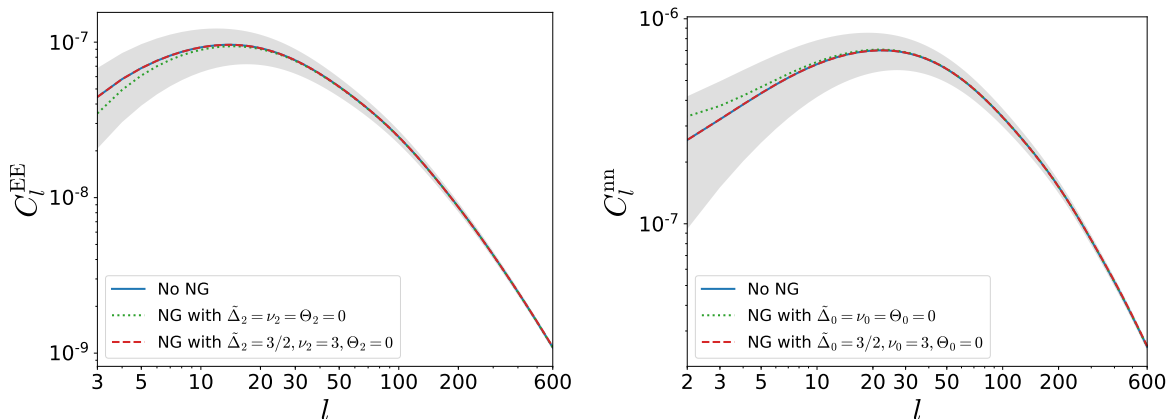


Figure 1. These plots show the angular auto-power spectra C_l^{EE} (Left) and C_l^{nn} (Right) for initial conditions with different PNGs. The blue solid lines show the case with $\bar{b}_{\text{NG}}^{\text{I}} A_2 = 0$ (Left) and $A_0 = 0$ (Right), including the Gaussian initial condition. In the left panel, the green dotted line shows the case with $\bar{b}_{\text{NG}}^{\text{I}} A_2 = 100$ and $\tilde{\Delta}_2 = \nu_2 = \Theta_2 = 0$ and the red dashed line shows the case with $\bar{b}_{\text{NG}}^{\text{I}} A_2 = 8 \times 10^3$, $\tilde{\Delta}_2 = 3/2$, $\nu_2 = 3$, and $\Theta_2 = 0$. In the right panel, the green dotted line shows the case with $A_0 = 10$ and $\tilde{\Delta}_0 = \nu_0 = \Theta_0 = 0$ and the red dashed line shows the case with $A_0 = 8 \times 10^3$, $\tilde{\Delta}_0 = 3/2$, $\nu_0 = 3$, and $\Theta_0 = 0$. The shaded regions show the noise due to the cosmic variance computed for the Gaussian initial condition. Here, we set z_{*a} with $a = \text{I, G}$ as $z_{*\text{I}} = z_{*\text{G}} = 0.3$.

of Fig. 1 shows the angular power spectrum of δ_{n} for the three different initial conditions: $A_0 = 0$ (Blue), $A_0 = 10$, $\tilde{\Delta}_0 = \nu_0 = \Theta_0 = 0$ (Green dotted), and $A_0 = 8000$, $\tilde{\Delta}_0 = 3/2$, $\nu_0 = 3$, $\Theta_0 = 0$ (Red dashed). The imprint of the PNG with $A_0 \neq 0$ on C_l^{nn} appears in a similar way to the one of the PNG with $A_2 \neq 0$ on C_l^{EE} . In Fig. 1, we set the non-Gaussian parameters $\bar{b}_{\text{NG}}^{\text{I}} A_2$ and A_0 to those which roughly amount to the 1- σ uncertainties obtained in Sec. 3.3. The deviations of the cases with $\tilde{\Delta}_s = 3/2$ (the red dashed lines) from the Gaussian case (the blue solid lines), which are not visible in Fig. 1, are manifestly shown in Fig. 2.

While the angular power spectrum C_l^{EE} starts with the quadrupole component, in the left panel of Fig. 1, we only plotted C_l^{EE} with $l \geq 3$. For $l = 2$, taking the limit $x = k\chi \ll 1$, we find that the contribution of the PNG in C_2^{EE} given by Eq. (3.6) is proportional to $\int d^3k P_\phi(k)$ [13], letting thus computed C_2^{EE} sensitive to the fluctuations at scales which are much larger than the Hubble scale of our universe. This requires us to reconsider the expression of C_2^{EE} given by Eq. (3.6) more carefully. Leaving this subtle issue for a future study, here we only consider C_l^{EE} with $l \geq 3$. For the auto-correlation of δ_{n} , we plotted C_l^{nn} with $l \geq 2$, including the quadrupole contribution.

Since $\mathcal{M}(k, z)$ scales as k^2 in the limit $k \rightarrow 0$, for $\tilde{\Delta}_2 = 0$, the second terms of $b_{\text{eff}}^{\text{I}}(z, k)$ and $b_{\text{eff}}^{\text{n}}(z, k)$ become larger at larger scales, leading the relative enhancement for small ls . On the other hand, for $\tilde{\Delta}_2 = 3/2$, the enhancement at the low multipoles are not significant. Instead, the imprint of the PNG becomes more and more significant at higher multipoles. This can be understood as follows. For $k \gg k_{\text{eq}}$, where k_{eq} denotes the comoving Hubble scale at the matter-radiation equality and is given by $k_{\text{eq}} \simeq 1.6 \times 10^{-2} h/\text{Mpc}$, $\mathcal{M}(z, k)$ ceases to depend on k . Therefore, in the range $k \gg k_{\text{eq}}$, the second terms of $b_{\text{eff}}^{\text{I}}(z, k)$ and $b_{\text{eff}}^{\text{n}}(z, k)$ can dominate the first terms for $\tilde{\Delta}_2 > 0$ and $\tilde{\Delta}_0 > 0$, respectively. For the higher multipoles on which the information of the modes $k > k_{\text{eq}}$ is encoded, using the Limber approximation,

we find that the auto-correlations of the contributions from the PNG scale as

$$C_l^{\text{EE,PNG}} \propto l^{2\tilde{\Delta}_2-3+n_s-1}, \quad C_l^{\text{nn,PNG}} \propto l^{2\tilde{\Delta}_0-3+n_s-1}, \quad (3.16)$$

where n_s is the spectral index for the adiabatic perturbation. (Here, dropping the oscillatory contributions, we only picked up the powers of l .) Therefore, especially for $\tilde{\Delta}_s \simeq 3/2$ with $s = 0, 2$, the contributions from the PNG in the angular spectra stay almost constant at the higher multipoles in contrast to the linear contributions which are suppressed.

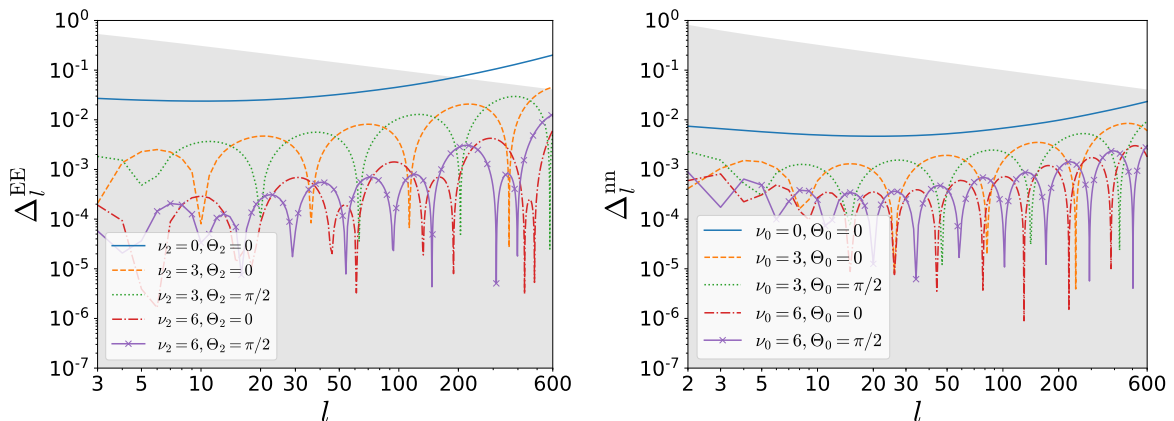


Figure 2. These plots show the fractional changes Δ_l^α , defined in Eq. (3.17), for $\alpha = \text{EE}$ (left) and for $\alpha = \text{nn}$ (Right). The parameters $\tilde{\Delta}_0$ and $\tilde{\Delta}_2$ are both chosen to be $3/2$. In the left panel, $\bar{b}_{\text{NG}}^1 A_2$ is set to $\bar{b}_{\text{NG}}^1 A_2 = 8000$ and in the right panel, A_0 is set to $A_0 = 8000$. The shaded regions show the variance computed by taking into account the cosmic variance. Here, we set z_{*a} with $a = \text{I, G}$ as $z_{*\text{I}} = z_{*\text{G}} = 0.3$.

To exhibit the enhancements of the contribution from the PNG at the high multipoles more clearly, in Fig. 2, we plot the fractional changes of C_l^{EE} and C_l^{nn} which quantify the contributions from the PNG as

$$\Delta_l^\alpha \equiv \frac{|C_l^\alpha - C_{l,\text{Gauss}}^\alpha|}{C_{l,\text{Gauss}}^\alpha} \quad (\alpha = \text{EE, nn}), \quad (3.17)$$

where $C_{l,\text{Gauss}}^\alpha$ denotes the angular power spectrum computed for the Gaussian initial condition. The different lines show the PNG with the different periodic oscillations and the phases. Notice that there is a phase difference between Δ_l^{EE} and Δ_l^{nn} with the same oscillatory period, i.e., $\nu_2 = \nu_0$, and the phase, i.e., $\Theta_2 = \Theta_0$. This is because the E-mode cosmic shear is contaminated by the lensing effect, whose correlation with the intrinsic contribution leads to the anti-correlation, and also because the integrands in Eqs. (3.6) and (3.8) have different powers of k for each multipole l .

In Ref. [22], the modification of the halo bias due to the presence of the PNG with $A_0 \neq 0$ and $0 \leq \tilde{\Delta}_0 \leq 2$ was computed. It was shown that for a larger $\tilde{\Delta}_0$, the signal of the PNG appears in the small scales (see also Ref. [57]). Here, we have shown that the signal of the PNG with $A_2 \neq 0$ and $\tilde{\Delta}_2 = 3/2$ also becomes more prominent at higher multipoles which capture the contributions of the modes $k > k_{\text{eq}}$.

For $\tilde{\Delta}_s = 0$, the information of the PNG is encoded in large scale fluctuations. Therefore, a detection of such a PNG is usually limited by the cosmic variance. On the other hand, for a

larger value of $\tilde{\Delta}_s$, the situation becomes very different, since the signal of the PNG appears in small scales. For an accurate computation, we need to include non-linear evolution. This is left for our future study [58].

3.3 Fisher matrix analysis

In this section, we study how well future observations will be able to constrain the model parameters by using the Fisher matrix formalism (see e.g., Refs. [59–61]). The Fisher information matrix is given by

$$F_{ij} = \sum_l \frac{(2l+1)f_{\text{sky}}}{2} \text{Tr} \left(\mathbf{C}^{-1} \frac{\partial \mathbf{C}}{\partial p_i} \mathbf{C}^{-1} \frac{\partial \mathbf{C}}{\partial p_j} \right), \quad (3.18)$$

with the covariance matrix

$$\mathbf{C}(l) \equiv \begin{pmatrix} C_l^{\text{nn}} & C_l^{\text{nE}} \\ C_l^{\text{nE}} & C_l^{\text{EE}} \end{pmatrix}. \quad (3.19)$$

Here, p_i is a model parameter. Recall that in this section, we consider the case with the parity symmetry and the global rotational symmetry, which lead to the absence of the B-mode and correlations among different multipoles.

As a noise effect, here we consider the shot noise which we assume to be white spectrum as

$$N^{\text{EE}} = \frac{\sigma_\gamma^2}{\bar{n}_\text{G}}, \quad N^{\text{nn}} = \frac{1}{\bar{n}_\text{n}}, \quad N^{\text{nE}} = 0, \quad (3.20)$$

where σ_γ^2 is the dispersion of the intrinsic shape with instrumental noise per component, \bar{n}_G is the projected surface density of galaxies with shapes per steradian, and \bar{n}_n is the galaxies clustering density per steradian. We include this noise effect, changing the angular power spectra in Eq. (3.19) as

$$C_l^\alpha \rightarrow C_l^\alpha + N_l^\alpha, \quad (\alpha = \text{EE}, \text{nn}, \text{nE}). \quad (3.21)$$

In the following, considering a noise estimation for an LSST-like measurement [5, 51], we use $f_{\text{sky}} = 0.5$, $\bar{n}_\text{G} = 37/\text{arcmin}^2$, $\bar{n}_\text{n} = 46/\text{arcmin}^2$, and $\sigma_\gamma = 0.25$.

The present setup includes the parameters

$$\{b_1^{\text{n}}, \bar{b}_1^{\text{I}}, A_0, \bar{b}_{\text{NG}}^{\text{I}} A_2, \mathcal{A}_s\}, \quad (3.22)$$

where \mathcal{A}_s is the amplitude of the scalar power spectrum at the pivot scale $k_p = 0.05 \text{Mpc}^{-1}$, and the parameters

$$\{\tilde{\Delta}_0, \nu_0, \Theta_0, \tilde{\Delta}_2, \nu_2, \Theta_2\}, \quad (3.23)$$

which characterize the scale dependence of $b_{\text{eff}}^{\text{I}}(z, k)$ and $b_{\text{eff}}^{\text{n}}(z, k)$. Since $\bar{b}_{\text{NG}}^{\text{I}}$ and A_2 entirely degenerate, here we take $\bar{b}_{\text{NG}}^{\text{I}} A_2$ as a single parameter. In the following, considering a certain model of inflation, we fix the parameters (3.23) to specific values. In particular, we consider the PNGs which are generated in two different inflation models:

1. Inflation model with multi-light scalar fields and a massive spin-2 field in the principal series coupled with the inflaton, where the PNG with $A_0, A_2, \nu_2 \neq 0$ and $\tilde{\Delta}_0 = \nu_0 = \Theta_0 = 0$ and $\tilde{\Delta}_2 = 3/2$ can be generated⁵.
2. Inflation model with a massive scalar field and a massive spin-2 field which are both in the principal series and are both coupled with the inflaton, where the PNG with $A_0, A_2, \nu_0, \nu_2, \neq 0$ and $\tilde{\Delta}_0 = \tilde{\Delta}_2 = 3/2$ can be generated.

Here, marginalizing over other parameters, we discuss a possible constraint on the parameters $p_1 \equiv A_0$ and $p_2 \equiv \bar{b}_{\text{NG}}^{\text{I}} A_2$. When all other parameters, leaving aside either of p_1 or p_2 , are fully marginalized, the 1σ bound on p_i is given by $\sigma(p_i) = \sqrt{(\mathbf{F}^{-1})_{ii}}$ (see e.g., Ref. [59]). Here, we choose the fiducial values of the parameters (3.22) as

$$(b_1^n, \bar{b}_1^{\text{I}}, A_0, \bar{b}_{\text{NG}}^{\text{I}} A_2, \mathcal{A}_s) = (2, -0.1, 0, 0, 2.2 \times 10^{-9}),$$

where the fiducial value of \mathcal{A}_s is set to the best fit value of Planck 15 [28]. For the Fisher analysis, we use the angular power spectra with $3 \leq l \leq 600$. Table 1 and Table 2 show the 1σ uncertainties of p_i ($i = 1, 2$) for the model 1 and the model 2, respectively.

$\nu_2 = 3$	$\sigma(f_{\text{NL}}^{\text{loc}})$	$\sigma(\bar{b}_{\text{NG}}^{\text{I}} A_2)$	$\nu_2 = 6$	$\sigma(f_{\text{NL}}^{\text{loc}})$	$\sigma(\bar{b}_{\text{NG}}^{\text{I}} A_2)$
$\Theta_2 = 0$	1.9	7.5×10^3	$\Theta_2 = 0$	1.9	2.1×10^4
$\Theta_2 = \pi/2$	1.9	7.1×10^3	$\Theta_2 = \pi/2$	1.9	2.5×10^4

Table 1. 1σ uncertainties of the non-Gaussian parameters A_0 and $\bar{b}_{\text{NG}}^{\text{I}} A_2$ for the model 1 with the other parameters fully marginalized. The parameter ν_2 was set to $\nu_2 = 3$ (Left) and $\nu_2 = 6$ (Right). Here, considering an LSST-like measurement, we set z_{*a} with $a = \text{I, G}$ as $z_{*\text{I}} = z_{*\text{G}} = 0.51$. Adjusting to the convention, we used $f_{\text{NL}}^{\text{loc}}$, which is related to A_0 as $f_{\text{NL}}^{\text{loc}} = A_0/4$.

$\nu_{0,2} = 3$	$\sigma(A_0)$	$\sigma(\bar{b}_{\text{NG}}^{\text{I}} A_2)$	$\nu_{0,2} = 6$	$\sigma(A_0)$	$\sigma(\bar{b}_{\text{NG}}^{\text{I}} A_2)$
$\Theta_{0,2} = 0$	3.5×10^3	1.0×10^4	$\Theta_{0,2} = 0$	7.4×10^3	3.1×10^4
$\Theta_{0,2} = \pi/2$	4.3×10^3	1.0×10^4	$\Theta_{0,2} = \pi/2$	8.7×10^3	3.7×10^4

Table 2. The same as Table 1 for the model 2. The parameter ν_0 and ν_2 were set to $\nu_0 = \nu_2 = 3$ (Left) and $\nu_0 = \nu_2 = 6$ (Right). For simplicity, we choose the same value for the phases Θ_0 and Θ_2 .

In order to examine a possible degeneracy among the non-Gaussian parameters, we also compute a partially marginalized bound on the parameters p_i ($i = 1, 2$), using the submatrix $(\mathbf{F}^{-1})_{i=[1,2],j=[1,2]}$. Here, we marginalize only over the parameters $\{b_1^n, \bar{b}_1^{\text{I}}, \mathcal{A}_s\}$. The result is in Fig. 3. As is shown in the left panel, there is almost no degeneracy between $f_{\text{NL}}^{\text{loc}}$ and $\bar{b}_{\text{NG}}^{\text{I}} A_2$. This is because $f_{\text{NL}}^{\text{loc}}$ contributes to low ls , but $\bar{b}_{\text{NG}}^{\text{I}} A_2$ contributes to high ls . On the other hand, as is shown in the right panel, there is some degeneracy between A_0 and $\bar{b}_{\text{NG}}^{\text{I}} A_2$, because both of them contribute to high ls ⁶. (A correlation between the PNGs from fields with different spins was discussed in Ref. [65].)

⁵As was argued in Refs. [62, 63], $f_{\text{NL}}^{\text{loc}}$ is suppressed in single clock models of inflation.

⁶Our constraint on $f_{\text{NL}}^{\text{loc}}$ is much tighter than the one in Ref. [13]. This is mainly because our redshift distribution dN_n/dz extends to higher redshift region than the one used in Ref. [13]. In fact, when we use the redshift distribution for LSST red samples [64] and set $\bar{n}_{\text{I}}, \bar{n}_{\text{G}}$ and \bar{n}_{n} to the values used in Ref. [13], i.e., $\bar{n}_{\text{I}} = \bar{n}_{\text{G}} = 3$ and $\bar{n}_{\text{n}} = 26$, we obtain $\sigma(f_{\text{NL}}^{\text{loc}}) = 8.3$, $\sigma(\bar{b}_{\text{NG}}^{\text{I}} A_2) = 3.0 \times 10^3$ for $\nu_2 = 3$ and $\Theta_2 = 0$. Now, $\sigma(f_{\text{NL}}^{\text{loc}}) = 8.3$ is almost same as the one in Ref. [13].

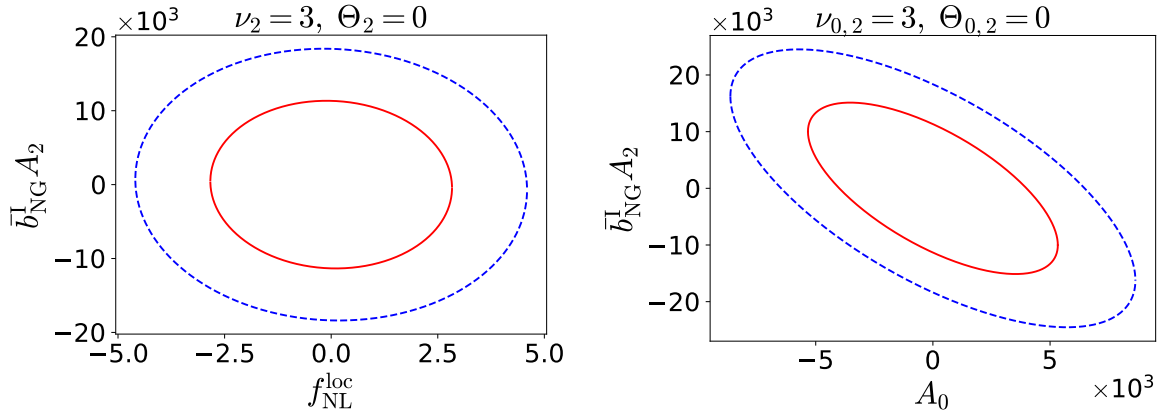


Figure 3. These plots show 1- σ and 2- σ uncertainties in the non-Gaussian parameters A_0 and $\bar{b}_{\text{NG}}^I A_2$, when we marginalize over $\{b_1^n, \bar{b}_1^I, \mathcal{A}_s\}$. The red solid lines show the 1- σ contours and the blue dotted lines show the 2- σ contours. The left panel is the model 1 (with $\tilde{\Delta}_0 = \nu_0 = \Theta_0 = 0$ and the right one is the model 2 (with $\tilde{\Delta}_0 = 3/2$). Other parameters are set to $\tilde{\Delta}_2 = 3/2$, $\nu_2 = 3$, $\Theta_2 = 0$ (Left) and $\tilde{\Delta}_0 = \tilde{\Delta}_2 = 3/2$, $\nu_0 = \nu_2 = 3$, $\Theta_0 = \Theta_2 = 0$ (Right).

The constraint on A_0 with $\nu_0 = \Theta_0 = 0$, so no oscillatory feature, was discussed in Ref. [22], including also the non-linear loop corrections. As is shown in Fig. 2, the enhancement due to the PNG becomes less significant for a larger value of ν_s , since the oscillatory contribution is more smoothed out by integrating over k . Because of that, constraints for $\nu_0 = \nu_2 = 6$ become weaker than those for $\nu_0 = \nu_2 = 3$.

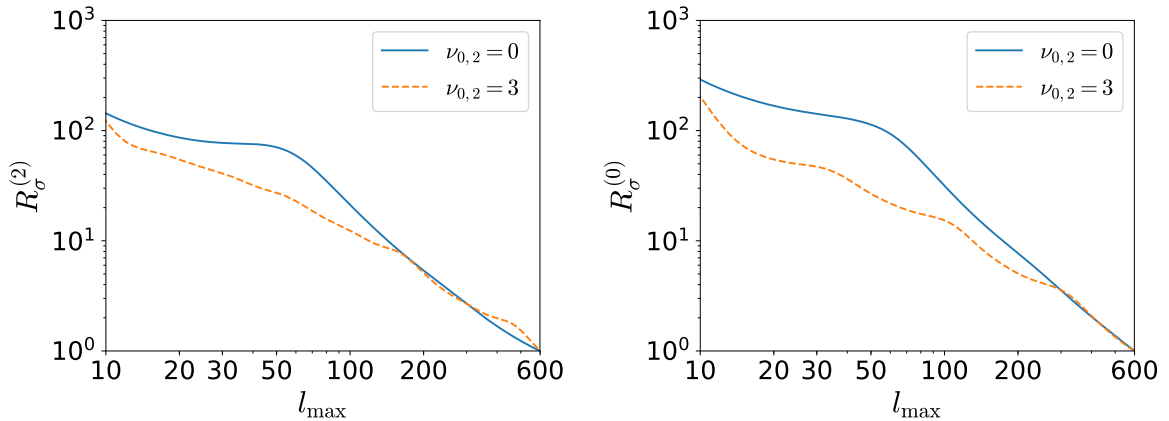


Figure 4. The left and right panels show $R_\sigma^{(2)}$ and $R_\sigma^{(0)}$, respectively, which are defined in Eq. (3.24). The blue solid lines show the case with $\nu_0 = \nu_2 = 0$ and the orange dotted lines show the case with $\nu_0 = \nu_2 = 3$. For both cases, we set $\Theta_0 = \Theta_2 = 0$.

When $\tilde{\Delta}_s$ with $s = 0, 2$ are $3/2$, the dominant signals of the PNG come from the small scales with $k > k_{\text{eq}}$. Therefore, the possible constraints on the non-Gaussian parameters are highly sensitive to k_{max} or l_{max} . In Fig. 4, to see the l_{max} dependence of 1- σ uncertainty, we

plotted

$$R_\sigma^{(s)} \equiv \frac{\sigma_{3 \leq l \leq l_{\max}}(x_s)}{\sigma(x_s)} \quad s = 0, 2, \quad (3.24)$$

with $x_0 = A_0$ and $x_2 \equiv \bar{b}_{\text{NG}}^{\text{I}} A_2$. Here, $\sigma_{3 \leq l \leq l_{\max}}(x_s)$ denotes the 1- σ uncertainty when we only use $3 \leq l \leq l_{\max}$, i.e., $\sigma(x_s) = \sigma_{3 \leq l \leq 600}(x_s)$. For both $s = 0$ and $s = 2$, $R_{\sigma, \max}^{(s)}$ does not change much until around $l_{\max} = 100$ and it significantly drops for $l_{\max} \gtrsim 100$, approaching to 1.

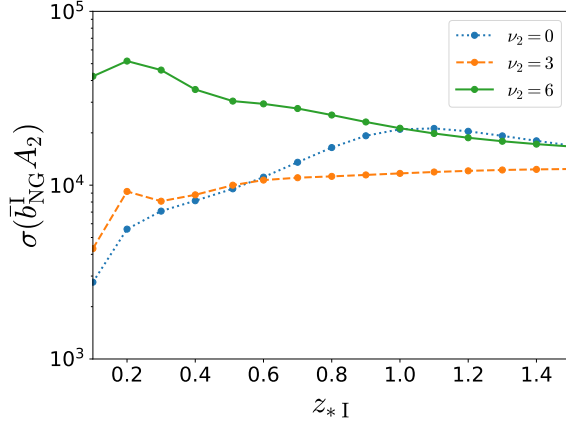


Figure 5. This plot shows how the 1- σ uncertainty of $\bar{b}_{\text{NG}}^{\text{I}} A_2$ changes under a variation of $z_{*I} = z_{*G}$ for different values of ν_2 . Here, we chose $\Theta_2 = 0$.

The forecast of 1- σ uncertainties in the non-Gaussian parameters also depends on the redshift distribution of galaxies dN_a/dz . Figure 5 shows a change of the 1- σ uncertainty for the parameter $\bar{b}_{\text{NG}}^{\text{I}} A_2$ under a variation of $z_{*I} (= z_{*G})$. As we change z_{*I} to a smaller value, the peaks of the linear spectra shift to lower multipoles, leaving more spaces for the PNG with $\tilde{\Delta}_s > 0$ to exhibit the signal at the high multipoles. Because of that, a galaxy survey which explores lower redshift tends to give a tighter constraint if it were to be no oscillation (see the plot with $\nu_2 = 0$). Notice however that $\sigma(\bar{b}_{\text{NG}}^{\text{I}} A_2)$ does not monotonically decrease as we decrease z_{*I} in the presence of the oscillation, i.e., $\nu_2 \neq 0$. It is because depending on the phase Θ_2 , the oscillation can reduce the signal of the PNG at the high multipoles at which the contribution from the PNG can dominate the linear contributions.

In the present analysis, we only considered a single tracer and integrated over the whole redshift distribution of galaxies, losing the information about modes along the line of sight (see also the discussion in Ref. [13]). Therefore, using tomographic information for multi tracers will improve our constraints on the non-Gaussian parameters. (For a multi-tracer analysis with $\tilde{\Delta}_2 = \nu_2 = 0$, see [20]. See also Ref. [50].)

4 Intrinsic alignment with global anisotropy

In the previous section, we showed that the angular dependent PNG generated from a massive spin-2 field can lead to the oscillatory feature in the intrinsic galaxy alignment, characterized by $b_{\text{eff}}^{\text{I}}(z, k)$, at small scales with $k > k_{\text{eq}}$. In this section, we discuss other sources of the

intrinsic alignment, focusing on whether there is a qualitative difference between their signals and the one discussed in the previous section.

4.1 Angular dependent PNG with global anisotropy

In the previous section, we discussed the intrinsic alignment generated from the angular dependent PNG which preserves the global rotation symmetry. Next, we consider the PNG (2.8) with a violation of the global rotational symmetry, which may be sourced from a vector field during inflation. Using Eqs. (2.10) and (2.11) and repeating a similar computation to the one in the previous section, we find that the PNG (2.8) yields the following contributions in the galaxy shape function g_{ij} :

$$g_{ij} \propto \left(\hat{p}_i \hat{p}_j - \frac{1}{3} \delta_{ij} \right) \phi, \quad \left(\hat{p}_i \partial_j + \hat{p}_j \partial_i - \frac{2}{3} \delta_{ij} \hat{p}^k \partial_k \right) \phi, \quad \dots, \quad (4.1)$$

which breaks the global rotational symmetry. The computation becomes somewhat lengthy and is summarized in Appendix A.

Including a typical contribution of the intrinsic alignment in the presence of the global anisotropy, here, we consider the case where the galaxy shape function is given by

$$g_{ij}(\mathbf{x}) = \int \frac{d^3 \mathbf{k}}{(2\pi)^{\frac{3}{2}}} e^{i\mathbf{k} \cdot \mathbf{x}} \left[b_1^I \left(\hat{k}_i \hat{k}_j - \frac{1}{3} \delta_{ij} \right) \delta(z, \mathbf{k}) + 3b_{\text{NG}}^p \bar{A}_2 \left(\frac{k}{k_*} \right)^{\Delta_p} \left(\hat{p}_i \hat{p}_j - \frac{1}{3} \delta_{ij} \right) \phi(\mathbf{k}) \right], \quad (4.2)$$

where b_{NG}^p denotes the bias parameter after the renormalization. (Here, we introduced the factor 3 for the non-Gaussian contribution, adjusting to the notation in the previous section.) For instance, when the primordial bispectrum is given by Eq. (2.8) with $\bar{A}_2 \neq 0$ and $\bar{B}_2 = \mathcal{O}((k_L/k_S))$, the leading contribution of g_{ij} takes the form of Eq. (4.2).

Meanwhile, any of galaxy surveys can probe only a finite spatial region in the universe. Because of that, even if the primordial bispectrum preserves the global isotropy, the limitation of the survey region can lead to an apparent anisotropic clustering of galaxy distributions, depending on the shape of the survey region [27] (see also Ref. [26]).

In the following, considering g_{ij} given by Eq. (4.2) without specifying the origin of the global anisotropy therein, we consider its observable imprints on the cosmic shear. We assume the power spectrum of ϕ with the global isotropy. (Recall that in a certain parameter range of the model in Ref. [24], the global anisotropy appears only from the bispectrum.)

Using the prescription in Sec. 2.3, we obtain the coefficient a_{lm}^{IA} for the expansion series of the intrinsic galaxy shear in terms of the spin weighted spherical harmonics as

$$a_{lm}^{\text{IA}} = 2\pi \sqrt{\frac{(l+2)!}{(l-2)!}} \int \frac{d^3 \mathbf{k}}{(2\pi)^{\frac{3}{2}}} \delta(\mathbf{k}) \sum_{s=-2}^2 F_{l,m}^{\text{IA},(s)}(k) i^{l+s} Y_{l+s,m}^*(\hat{\mathbf{k}}), \quad (4.3)$$

where $\delta(\mathbf{k})$ is the matter perturbation at present and $F_{l,m}^{\text{IA},(s)}(k)$ is given by

$$F_{l,m}^{\text{IA},(s)}(k) \equiv \int dz \frac{dN_I}{dz} \frac{D(z)}{D(0)} j_{l+s}(x) \times \left[-\frac{b_1^I}{x^2} \delta_{s,0} + 3b_{\text{NG}}^p \bar{A}_2 \left(\frac{k}{k_*} \right)^{\Delta_p} \mathcal{M}^{-1}(z, k) \frac{(l-2)!}{(l+2)!} \alpha_{l,m}^{(s)} \right]. \quad (4.4)$$

The detailed computation and the expression of $\alpha_{l,m}^{(s)}$ are summarized in Appendix B. Notice that the violation of the global rotational symmetry leads to the contamination of the different multipoles $l + s$ with $s = \pm 1, \pm 2$. The first term in the square brackets of Eq. (4.4) is the contribution which preserves the global rotational symmetry and the second term is the one which does not. The overall factor of the second term has the typical form of the scale dependent bias.

Notice that for the present pattern of the symmetry breaking, all of $\alpha_{l,m}^{(s)}$ vanish for $l = 0$ and $l = 1$. Therefore, the lowest multipole of the cosmic shear is still $l = 2$. Also notice that $\alpha_{l,m}$ takes a different value, depending on the value of m , and in particular, we find

$$\alpha_{l,-m}^{(s)} = \alpha_{l,m}^{(s)} \quad (s = 0, \pm 2), \quad \alpha_{l,-m}^{(s)} = -\alpha_{l,m}^{(s)} \quad (s = \pm 1). \quad (4.5)$$

In doing the harmonic expansion, we defined the z axis (with the colatitude angle $\theta = 0$) to be along the constant vector $\hat{\mathbf{p}}$. Some of the properties described here are specific for this coordinate choice (see Appendix B.2).

4.2 Angular power spectrum

Using a_{lm}^{IA} , given in Eq. (4.3), now we can compute the angular power spectrum of the cosmic shear. The second term in the left-hand side of Eq. (4.2) only contributes to the intrinsic alignment, leaving the perturbation of the number density and the gravitational lensing shear intact. Therefore, simply changing the contribution of the galaxy alignment into Eq. (4.3) in the computation of the previous section, we can obtain the angular power spectra as

$$\langle a_{lm}^X a_{l'm'}^{Y*} \rangle = C_{l,l';m}^{XY} \delta_{m,m'}, \quad (4.6)$$

where $X, Y = \text{n, E, B}$. Notice that since the parity symmetry is broken by the constant vector field \mathbf{p} , the B-mode cosmic shear takes a non-vanishing value. For instance, the auto-correlation of the B-mode is given by

$$\begin{aligned} C_{l,l';m}^{\text{BB}} &= \frac{1}{2\pi} \sqrt{\frac{(l-2)!}{(l+2)!}} \sqrt{\frac{(l'-2)!}{(l'+2)!}} (3b_{\text{NG}}^p \bar{A}_2)^2 \sum_{s=\pm 1} \sum_{s'=\pm 1} \delta_{l+s, l'+s'} \alpha_{l,m}^{(s)} \alpha_{l',m}^{(s')} \\ &\times \int dz \frac{dN_{\text{I}}}{dz} \int dz' \frac{dN_{\text{I}}}{dz'} \int dk k^2 j_{l+s}(k\chi(z)) j_{l'+s'}(k\chi(z')) \left(\frac{k}{k_*}\right)^{2\Delta_p} P_\phi(k). \end{aligned} \quad (4.7)$$

Since there is no parity violation in the lensing contribution, the B-mode cosmic shear only appears from the intrinsic galaxy alignment. (Other origins of the B-mode cosmic shear were reported, e.g., in Refs. [66–68].)

Except for $X = Y = \text{n}$, on which the violation of the global rotational symmetry does not affect, $C_{l,l';m}$ has non-diagonal components on l . This is summarized in Table 3. We find that the auto-correlations $C_{l,l';m}^{\text{EE}}$ and $C_{l,l';m}^{\text{BB}}$ and the cross-correlation $C_{l,l';m}^{\text{EB}}$ take non-vanishing values, when $l - l'$ are even numbers. On the other hand, the cross-correlations $C_{l,l';m}^{\text{nE}}$ and $C_{l,l';m}^{\text{nB}}$ take non-vanishing values, when $l - l'$ are odd numbers. This is because a_{lm}^{E} consists of the density perturbation with $l, l \pm 2$ and a_{lm}^{B} consists of the one with $l \pm 1$. For a_{lm}^{n} , there is no mode coupling between different multipoles.

Figure 6 shows the auto-correlations of the E-mode and the B-mode, when the PNG is given by Eq. (2.2) with $\bar{A}_2 \neq 0$ and $\bar{B}_2 = \Delta_p = 0$. In this case, the galaxy shape function is given by Eq. (4.2) with $\Delta_p = 0$. For a comparison, we also plotted the angular spectra

$l' \backslash l$	$l-4$	$l-3$	$l-2$	$l-1$	l	$l+1$	$l+2$	$l+3$	$l+4$
$C_{l,l';m}^{EE}$	Red (solid)	0	Green (dashed)	0	Blue (dotted)	0	Red (dot-dashed)	0	Green (cross)
$C_{l,l';m}^{EB}$	0		0		0		0		0
$C_{l,l';m}^{BB}$	0	0	Red (solid)	0	Green (dashed)	0	Blue (dotted)	0	0
$C_{l,l';m}^{mE}$	0	0		0		0		0	0
$C_{l,l';m}^{mB}$	0	0	0		0		0	0	0

Table 3. For the components which identically vanish, we put 0, otherwise non-zero. The modes with colour descriptions are shown in those colours in Fig. 7, which shows the auto-correlations of the E-mode and the B-mode.

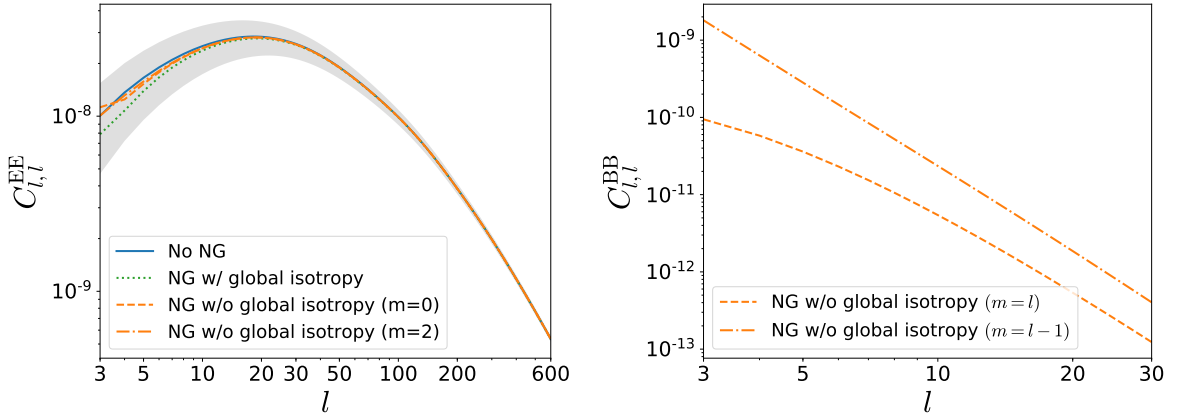


Figure 6. The left panel shows the E-mode cosmic shear and the right panel shows the B-mode cosmic shear for three cases; the blue solid line shows the case with the Gaussian initial condition, the green dotted line shows the case with the PNG (2.2) with $A_2 \neq 0$ and $\tilde{\Delta}_2 = \nu_2 = \Theta_2 = 0$, and finally the orange dashed and dot-dashed lines show the case with the PNG (2.8) with $\tilde{A}_2 \neq 0$ and $\tilde{B}_2 = \Delta_p = 0$. The non-Gaussian parameters are set to $\bar{b}_{\text{NG}}^l A_2 = \bar{b}_{\text{NG}}^p \tilde{A}_2 = 100$. In the first two cases, the global rotational symmetry is preserved, while it is broken in the last one. The angular power spectra for the PNG (2.8) has the non-diagonal components of l and the azimuthal dependence. Here, we only plot the power spectra with $l = l'$. We plotted $m = 0$ and $m = 2$ for the E-mode and $m = l$ and $m = l - 1$ for the B-mode. Here, we set $z_{*I} = z_{*G} = 0.51$.

for the Gaussian initial condition and also for the PNG (2.2), which preserves the global rotation symmetry, with $A_2 \neq 0$ and $\tilde{\Delta}_2 = \nu_2 = \Theta_2 = 0$. In this computation, we choose the bias parameters in the same way as in the previous section, i.e., (3.14) and $b_{\text{NG}}^p = \bar{b}_{\text{NG}}^p \bar{b}_1^l \Omega_{m0}$ with $\bar{b}_1^l = -0.1$. Here, other bias parameters are irrelevant. The PNG (2.8) leads to the enhancement of the E-mode at large scales likewise the PNG (2.2) with $\tilde{\Delta}_2 = 0$. When we increase $\tilde{\Delta}_2$ or Δ_p , the signal from the PNG shows up at higher multipoles as was discussed in the previous section. Because of the parity violation in the galaxy alignment, the B-mode takes a non-vanishing value and is enhanced especially at low multipoles. Here, again we

removed $l = l' = 2$, which are also affected by the super Hubble contributions.

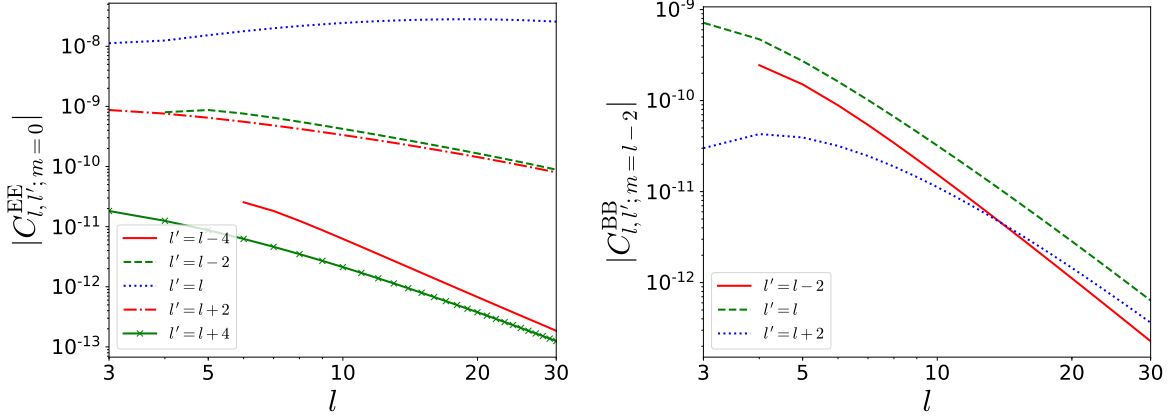


Figure 7. The angular power spectra of the E-mode (Left) and the B-mode (Right) for the diagonal and non-diagonal components. The left panel is the E mode auto-correlation with $m = m' = 0$. The right one is the B mode auto-correlation with $m = m' = l - 2$. The non-Gaussian parameters are set to $\bar{b}_{\text{NG}}^{\text{I}} A_2 = \bar{b}_{\text{NG}}^{\text{p}} \bar{A}_2 = 100$. Here, we set $z_{\text{I}} = z_{*G} = 0.51$.

Figure 7 shows the angular power spectra of the E-mode and the B-mode for the diagonal and non-diagonal components of ls . For the E-mode, we find that the diagonal component with $l = l'$ takes a larger amplitude than the non-diagonal components with $l - l' = \pm 2$ and $l - l' = \pm 4$ and among the non-diagonal components, the former takes a larger amplitude than the latter. This can be understood by focusing on the contributions of the linear alignment term and the lensing term. They do not contribute to $C_{l,l';m}^{\text{EE}}$ with $l - l' = \pm 4$ and contribute to the one with $l - l' = \pm 2$ only as the cross-correlation with the term from the PNG.

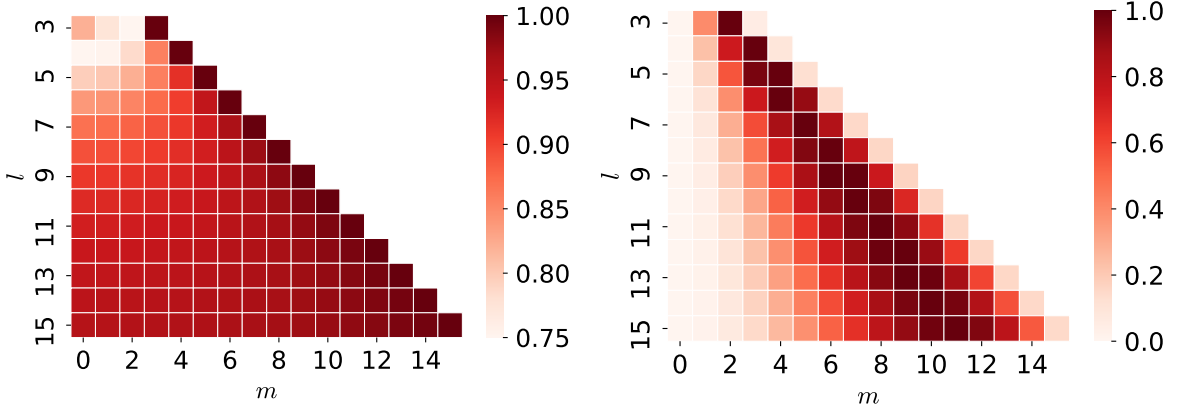


Figure 8. The left panel shows the azimuthal dependence for $C_{l,l';m}^{\text{EE}}$ and the right one shows the same for $C_{l,l';m}^{\text{BB}}$. Here, the angular power spectra are normalized by the maximum values for each l . Here, we set $z_{*I} = z_{*G} = 0.51$.

As another consequence of the violation of the global rotational symmetry, the angular power spectra (other than C^{mn}) take different values for different ms . This is summarized

in Fig. 8, which shows the azimuthal dependence of $C_{l,l';m}^{\text{EE}}$ and $C_{l,l';m}^{\text{BB}}$ with $l = l'$. Notice that the azimuthal modes m which are highly asymmetric lead to the larger parity violation, generating larger values of $C_{l,l';m}^{\text{BB}}$. In fact, $C_{l,l';m}^{\text{BB}}$ vanishes for $m = 0$. In contrast, $C_{l,l';m}^{\text{EE}}$ takes non-vanishing values for all azimuthal modes and the amplitude does not change as much as $C_{l,l';m}^{\text{BB}}$ does.

5 Conclusion

The angular dependent primordial non-Gaussianity (PNG), which can be generated from massive non-zero spin fields during inflation, serves a source of the intrinsic galaxy alignment. Especially for $\tilde{\Delta}_s = 3/2$, which is usually the case for massive fields (without an introduction of non-trivial interactions to sustain against the dilution), the signal of the PNG becomes more and more significant at small scales with $k > k_{\text{eq}}$. This is in sharp contrast to the signal from the PNG with $\tilde{\Delta}_s = 0$, which includes the squeezed bispectrum parametrized by $f_{\text{NL}}^{\text{loc}}$. Since the scale dependent bias generated from the PNG with $\tilde{\Delta}_s = 0$ is mainly enhanced at large scales, the detection is severely limited by the cosmic variance, while this problem may be somewhat circumvented by using multi-tracers [18, 19]. (See also Ref. [69].) On the other hand, since the signal from the massive fields appears in small scales, the issue of the cosmic variance is not crucial for the detection. Moreover, the distinctive oscillatory feature may allow us to discriminate from other contributions. These aspects are common for massive fields irrespective of their spins.

In this paper, we did not take into account the non-linear time evolution. Obviously, this is not sufficient to estimate the signal in the small scales accurately. We will report our computation which takes into account the non-linear clustering in our forthcoming paper [58]. Since these non-linear effects act as contaminations, the constraints on the PNG from massive particles, whose imprint is prominent at small scales, will become weaker unless we are able to subtract them out. (For other effects which are not considered here, see Ref. [13].)

The intrinsic galaxy alignment also can be generated from the angular dependent PNG which violates the global rotational invariance. When the galaxy shape function g_{ij} has the contribution which violates the global rotational symmetry, we find the following three distinctive consequences: i) Non-zero B-mode cosmic shear ii) Correlations between different multipoles l (depending on the choice of the z axis, there also appear correlations between different ms) iii) Azimuthal dependence of angular spectra. These aspects provide qualitative differences from the case with the angular dependent PNG (2.2).

In this paper, in computing the cosmic shear, we simply used the redshift distribution of the galaxy sample given in Ref. [51]. While the intrinsic alignment for red galaxies is observationally confirmed, the intrinsic alignment of blue galaxies has been observed to be null consistent (see, e.g., Ref. [16]). For a more realistic computation, we will need to choose the redshift distribution of the galaxy sample more carefully. As was discussed in Sec. 3.3, the forecast of the parameter uncertainty changes depending on a choice of the redshift distribution function of galaxies.

Acknowledgments

We would like to thank K. Akitsu, J. Miralda Escudé, J. Soda, M. Takada, F. Schmidt and A. Taruya for their fruitful comments and feedback. A. N. is in part supported by MEXT KAKENHI Grant under Contract No. 16H01096 and T. M. is supported by JSPS

Grant-in-Aid for Scientific Research (C) under Contract No. 15K05074, JSPS Grant-in-Aid for Scientific Research (B) under Contract No. 16H03977, and MEXT KAKENHI under Contract No. 15H05890. Y. U. is supported by JSPS Grant-in-Aid for Research Activity Start-up under Contract No. 26887018, Grant-in-Aid for Scientific Research on Innovative Areas under Contract No. 16H01095, and Grant-in-Aid for Young Scientists (B) under Contract No. 16K17689. Y. U. is also supported in part by Building of Consortia for the Development of Human Resources in Science and Technology and Daiko Foundation.

A Derivation of scale dependent bias

In this Appendix, following Ref. [13], we derive the scale dependent bias for g_{ij} and δ_n in the presence of the PNG with the global anisotropy (2.8). Here, the constant vector $\hat{\mathbf{p}}$ is left arbitrary. Here, for simplicity, we use the PNG (2.8) with $\Delta_p = 0$, but an extension to $\Delta_p \neq 0$ proceeds straightforwardly.

A.1 Galaxy shape

To compute the scale dependent bias $b_{\text{eff}}^{\text{I}}(z, k)$, we compute the two point function $\langle \delta(\mathbf{x})g_{ij}(\mathbf{y}) \rangle$. Using Eq. (2.11), we find that this two point function includes the three-point functions

$$\langle \delta(\mathbf{x})\delta(\mathbf{y})K_{ij}(\mathbf{y}) \rangle \quad \text{and} \quad \left\langle \delta(\mathbf{x}) \left[K_{ik}K_j^k - \frac{1}{3}\delta_{ij}(K_{lm})^2 \right] (\mathbf{y}) \right\rangle. \quad (\text{A.1})$$

Here, we compute the contribution of the squeezed bispectrum to the first term. Using the primordial bispectrum, defined as

$$\langle \phi_{\mathbf{k}_1}\phi_{\mathbf{k}_2}\phi_{\mathbf{k}_L} \rangle = (2\pi)^{-\frac{3}{2}}\delta(\mathbf{k}_1 + \mathbf{k}_2 + \mathbf{k}_L)B_\phi(\mathbf{k}_1, \mathbf{k}_2, \mathbf{k}_L), \quad (\text{A.2})$$

the first term can be rewritten as

$$\begin{aligned} \langle \delta(\mathbf{x})\delta(\mathbf{y})K_{ij}(\mathbf{y}) \rangle &\approx \int \frac{d^3\mathbf{k}_L}{(2\pi)^3} e^{i\mathbf{k}_L \cdot \mathbf{r}} \mathcal{M}(k_L) \int \frac{d^3\mathbf{k}_1}{(2\pi)^3} \left[\frac{k_{1i}k_{1j}}{k_1^2} - \frac{1}{3}\delta_{ij} \right] \\ &\quad \times \mathcal{M}(k_1)\mathcal{M}(|\mathbf{k}_1 + \mathbf{k}_L|)B_\phi(\mathbf{k}_1, -(\mathbf{k}_1 + \mathbf{k}_L), \mathbf{k}_L), \end{aligned} \quad (\text{A.3})$$

where \mathbf{k}_1 corresponds to the short mode. Since we only take into account the contribution from the squeezed configuration, we used \approx instead of the equality. Expanding this three-point function in terms of $q = k_L/k_S \ll 1$, we obtain

$$\begin{aligned} \langle \delta(\mathbf{x})\delta(\mathbf{y})K_{ij}(\mathbf{y}) \rangle &\approx \int \frac{d^3\mathbf{k}_L}{(2\pi)^3} e^{i\mathbf{k}_L \cdot \mathbf{r}} \mathcal{M}(k_L) \int \frac{d^3\mathbf{k}_S}{(2\pi)^3} \left[\frac{k_{Si}k_{Sj}}{k_S^2} - \frac{1}{3}\delta_{ij} \right] \\ &\quad \times \mathcal{M}^2(k_S)P_\phi(k_L)P_\phi(k_S) \sum_{l=0}^{\infty} [\bar{A}_l + \bar{B}_l\mu + \mathcal{O}(q)] i^{\frac{1-(-1)^l}{2}} \mathcal{P}_l(\hat{\mathbf{p}} \cdot \hat{\mathbf{k}}_S), \end{aligned} \quad (\text{A.4})$$

with $\mu = \hat{\mathbf{k}}_S \cdot \hat{\mathbf{k}}_L$. Here, we used $\mathcal{M}(|\mathbf{k}_S + \mathbf{k}_L|) = \mathcal{M}(k_S) + \mathcal{O}(q)$.

For our computational convenience, we change the coordinate system such that \mathbf{p} lies along the z axis as $\tilde{p}^i = \mathcal{R}^i_j(\hat{\mathbf{p}})p^j = (0, 0, \tilde{p})$, where $\mathcal{R}^i_j(\hat{\mathbf{p}})$ is a rotational matrix. Then, \mathbf{k}_S and \mathbf{k}_L are transformed into

$$\hat{\mathbf{k}}_a = \left(\sqrt{1 - \mu_a^2} \cos \psi_a, \sqrt{1 - \mu_a^2} \sin \psi_a, \mu_a \right), \quad (a = \text{L, S}) \quad (\text{A.5})$$

with

$$\mu = \hat{\mathbf{k}}_S \cdot \hat{\mathbf{k}}_L = \sqrt{(1 - \mu_S^2)(1 - \mu_L^2)} \cos(\psi_S - \psi_L) + \mu_S \mu_L, \quad (\text{A.6})$$

where we introduced $\mu_X \equiv \hat{\mathbf{p}} \cdot \hat{\mathbf{k}}_X$. In this coordinate, we obtain

$$\frac{\tilde{k}_{Si} \tilde{k}_{Sj}}{k_S^2} = \begin{pmatrix} \cos^2 \psi_S (1 - \mu_S^2) & \cos \psi_S \sin \psi_S (1 - \mu_S^2) & \cos \psi_S \mu_S \sqrt{1 - \mu_S^2} \\ \cos \psi_S \sin \psi_S (1 - \mu_S^2) & \sin^2 \psi_S (1 - \mu_S^2) & \sin \psi_S \mu_S \sqrt{1 - \mu_S^2} \\ \cos \psi_S \mu_S \sqrt{1 - \mu_S^2} & \sin \psi_S \mu_S \sqrt{1 - \mu_S^2} & \mu_S^2 \end{pmatrix}. \quad (\text{A.7})$$

Using this expression and integrating with respect to ψ_S , we obtain

$$\int_0^{2\pi} \frac{d\psi_S}{2\pi} \left[\hat{k}_{Si} \hat{k}_{Sj} - \frac{1}{3} \delta_{ij} \right] = \mathcal{P}_2(\mu_S) \left[\hat{p}_i \hat{p}_j - \frac{1}{3} \delta_{ij} \right], \quad (\text{A.8})$$

and

$$\begin{aligned} \int_0^{2\pi} \frac{d\psi_S}{2\pi} \mu \left[\hat{k}_{Sm} \hat{k}_{Sn} - \frac{1}{3} \delta_{mn} \right] &= \frac{1}{5} [\mathcal{P}_1(\mu_S) - \mathcal{P}_3(\mu_S)] \left[\hat{p}_m \hat{k}_{Ln} + \hat{p}_n \hat{k}_{Lm} - \frac{2}{3} \mu_L \delta_{mn} \right] \\ &+ \mu_L \mathcal{P}_3(\mu_S) \left[\hat{p}_m \hat{p}_n - \frac{1}{3} \delta_{mn} \right]. \end{aligned} \quad (\text{A.9})$$

Notice that as is shown Eq. (A.6), μ depends on μ_S , μ_L , ψ_S , and ψ_L . Using these formulae, Eq. (A.4) can be recast into

$$\begin{aligned} &\langle \delta(\mathbf{x}) \delta(\mathbf{y}) K_{ij}(\mathbf{y}) \rangle \\ &= \int \frac{d^3 \mathbf{k}_L}{(2\pi)^3} e^{i\mathbf{k}_L \cdot \mathbf{r}} \mathcal{M}(k_L) P_\phi(k_L) \int \frac{dk_S}{(2\pi)^2} k_S^2 \mathcal{M}^2(k_S) P_\phi(k_S) \\ &\quad \times \int_{-1}^1 d\mu_S \sum_{l=0}^{\infty} i^{\frac{1-(-1)^l}{2}} \mathcal{P}_l(\mu_S) \left\{ \left[\hat{p}_i \hat{p}_j - \frac{1}{3} \delta_{ij} \right] [\bar{A}_l \mathcal{P}_2(\mu_S) + \bar{B}_l \mu_L \mathcal{P}_3(\mu_S)] \right. \\ &\quad \left. + \frac{1}{5} \bar{B}_l [\mathcal{P}_1(\mu_S) - \mathcal{P}_3(\mu_S)] \left[\hat{p}_i \hat{k}_{Lj} + \hat{p}_j \hat{k}_{Li} - \frac{2}{3} \mu_L \delta_{ij} \right] + \mathcal{O}(q) \right\} \\ &= \int \frac{d^3 \mathbf{k}_L}{(2\pi)^3} e^{i\mathbf{k}_L \cdot \mathbf{r}} \mathcal{M}(k_L) P_\phi(k_L) \int \frac{dk_S}{(2\pi)^2} k_S^2 \mathcal{M}^2(k_S) P_\phi(k_S) \\ &\quad \times \frac{2}{5} \left\{ \frac{1}{3} i \bar{B}_1 \left[\hat{p}_i \hat{k}_{Lj} + \hat{p}_j \hat{k}_{Li} - \frac{2}{3} \mu_L \delta_{ij} \right] + \bar{A}_2 \left[\hat{p}_i \hat{p}_j - \frac{1}{3} \delta_{ij} \right] \right. \\ &\quad \left. + \frac{5}{7} i \bar{B}_3 \left[\mu_L \left[\hat{p}_i \hat{p}_j - \frac{1}{3} \delta_{ij} \right] - \frac{1}{5} \left(\hat{p}_i \hat{k}_{Lj} + \hat{p}_j \hat{k}_{Li} - \frac{2}{3} \mu_L \delta_{ij} \right) \right] + \mathcal{O}(q) \right\}. \end{aligned} \quad (\text{A.10})$$

Here, we used the orthogonality of the Legendre polynomials. Noticing the fact that the second term in Eq. (A.1) is related to the first term as

$$\left\langle \delta(\mathbf{x}) \left[K_{ik} K_{kj} - \frac{1}{3} \delta_{ij} (K_{lm})^2 \right] (\mathbf{y}) \right\rangle = \frac{1}{3} \langle \delta(\mathbf{x}) \delta(\mathbf{y}) K_{ij}(\mathbf{y}) \rangle + \mathcal{O}(q), \quad (\text{A.11})$$

we can immediately compute the second term.

Using

$$\xi(\mathbf{r}) = \int \frac{d^3 \mathbf{k}_L}{(2\pi)^3} e^{i\mathbf{k}_L \cdot \mathbf{r}} \mathcal{M}^2(k_L) P_\phi(k_L), \quad (\text{A.12})$$

$$\xi_{\delta\phi}(\mathbf{r}) = \int \frac{d^3 \mathbf{k}_L}{(2\pi)^3} e^{i\mathbf{k}_L \cdot \mathbf{r}} \mathcal{M}(k_L) P_\phi(k_L), \quad (\text{A.13})$$

$$\mathcal{I}(\mathbf{r}) = \int \frac{d^3 \mathbf{k}_L}{(2\pi)^3} e^{i\mathbf{k}_L \cdot \mathbf{r}} \frac{\mathcal{M}(k_L)}{k_L} P_\phi(k_L), \quad (\text{A.14})$$

and the variance of the matter density field $\langle \delta^2 \rangle$, given by

$$\langle \delta^2 \rangle = \int \frac{dk}{2\pi^2} k^2 \mathcal{M}^2(k) P_\phi(k), \quad (\text{A.15})$$

we finally obtain

$$\begin{aligned} \langle \delta(\mathbf{x}) g_{ij}(\mathbf{y}) \rangle &= b_1^I \mathcal{D}_{ij} \xi(\mathbf{r}) + \frac{1}{10} \bar{A}_2 (b_2^I + \frac{1}{3} b_t^I) \left(\hat{p}_i \hat{p}_j - \frac{1}{3} \delta_{ij} \right) \xi_{\delta\phi}(\mathbf{r}) \langle \delta^2 \rangle \\ &+ \mathcal{B}_1 \left(\hat{p}_i \hat{p}_j - \frac{1}{3} \delta_{ij} \right) \hat{\mathbf{p}} \cdot \partial_{\mathbf{x}} \mathcal{I}(\mathbf{r}) + \mathcal{B}_2 \left(\hat{p}_i \partial_j + \hat{p}_j \partial_i - \frac{2}{3} \delta_{ij} \hat{p}^k \partial_k \right) \mathcal{I}(\mathbf{r}), \end{aligned} \quad (\text{A.16})$$

where $\mathcal{B}_1, \mathcal{B}_2$ are

$$\mathcal{B}_1 \equiv \frac{1}{14} (b_2^I + \frac{1}{3} b_t^I) \bar{B}_3 \langle \delta^2 \rangle, \quad (\text{A.17})$$

$$\mathcal{B}_2 \equiv \frac{1}{210} (7\bar{B}_1 - 3\bar{B}_3) (b_2^I + \frac{1}{3} b_t^I) \langle \delta^2 \rangle. \quad (\text{A.18})$$

A.2 Number density

To compute the scale dependent bias $b_{\text{eff}}^n(z, k)$, we compute the two-point function $\langle \delta(\mathbf{x}) \delta_n(\mathbf{y}) \rangle$, which includes the three-point functions

$$\langle \delta(\mathbf{x}) \delta^2(\mathbf{y}) \rangle \quad \text{and} \quad \langle \delta(\mathbf{x}) (K_{ij})^2(\mathbf{y}) \rangle. \quad (\text{A.19})$$

The first term is given by

$$\begin{aligned} \langle \delta(\mathbf{x}) \delta^2(\mathbf{y}) \rangle &= \int \frac{d^3 \mathbf{k}_L}{(2\pi)^3} e^{i\mathbf{k}_L \cdot \mathbf{r}} \mathcal{M}(k_L) P_\phi(k_L) \int \frac{d^3 \mathbf{k}_S}{(2\pi)^3} \mathcal{M}^2(k_S) P_\phi(k_S) \\ &\times \sum_{\ell=0}^{\infty} i^{\frac{1-(-1)^\ell}{2}} [\bar{A}_\ell + \bar{B}_\ell \mu + \mathcal{O}(q)] \mathcal{P}_\ell(\mu_S), \end{aligned} \quad (\text{A.20})$$

where we used Eq. (2.8) and $\mathcal{M}(|\mathbf{k}_S + \mathbf{k}_L|) = \mathcal{M}(k_S) + \mathcal{O}(q)$. Since this formula does not depend on the azimuthal direction, μ in the square brackets can be simply replaced with $\mu_S \mu_L$ after integrating over ψ_S . Using the orthogonality of Legendre polynomials, we obtain

$$\begin{aligned} \langle \delta(\mathbf{x}) \delta^2(\mathbf{y}) \rangle &= \int \frac{d^3 \mathbf{k}_L}{(2\pi)^3} e^{i\mathbf{k}_L \cdot \mathbf{r}} \mathcal{M}(k_L) P_\phi(k_L) \int \frac{dk_S}{(2\pi)^2} k_S^2 \mathcal{M}^2(k_S) P_\phi(k_S) \\ &\times \left[2\bar{A}_0 + \frac{2}{3} i \mu_L \bar{B}_1 \right] + \mathcal{O}(q). \end{aligned} \quad (\text{A.21})$$

Using

$$\left[\widehat{k_{Si}} \widehat{k_{Sj}} - \frac{1}{3} \delta_{ij} \right] \left[\widehat{(k_S + k_L)}^i \widehat{(k_S + k_L)}^j - \frac{1}{3} \delta^{ij} \right] = \frac{2}{3} + \mathcal{O}(q^2), \quad (\text{A.22})$$

we also can compute $\langle \delta(\mathbf{x})(K_{ij})^2(\mathbf{y}) \rangle$ easily as $\langle \delta(\mathbf{x})(K_{ij})^2(\mathbf{y}) \rangle = \frac{2}{3} \langle \delta(\mathbf{x}) \delta^2(\mathbf{y}) \rangle + \mathcal{O}(q^2)$. Using these formulae, we obtain

$$\langle \delta(\mathbf{x}) \delta_n(\mathbf{y}) \rangle = b_1^n \xi(\mathbf{r}) + \frac{1}{2} \bar{A}_0 \langle \delta^2 \rangle (b_2^n + \frac{2}{3} b_t^n) \xi_{\delta\phi}(\mathbf{r}) + \frac{1}{6} \bar{B}_1 \langle \delta^2 \rangle (b_2^n + \frac{2}{3} b_t^n) \hat{\mathbf{p}} \cdot \partial_{\mathbf{x}} \mathcal{I}(\mathbf{r}). \quad (\text{A.23})$$

B Derivation and Feature of Angular power spectra

B.1 Calculation of intrinsic galaxy shape with global anisotropy

Here, we perform the harmonic expansion of the intrinsic alignment term in the cosmic shear. For our convenience, we decompose the contribution of the intrinsic alignment a_{lm}^{IA} as

$$a_{lm}^{\text{IA}} = a_{lm}^{(0)} + a_{lm}^{(p)},$$

where $a_{lm}^{(0)}$ is the contribution from the first term of Eq. (4.2) and $a_{lm}^{(p)}$ is the one from the second term. In the Fourier space, we obtain

$$\pm_2 \gamma^{\text{IA}}(z, \hat{\mathbf{n}}) = \int \frac{d^3 \mathbf{k}}{(2\pi)^{\frac{3}{2}}} e^{ix \hat{\mathbf{k}} \cdot \hat{\mathbf{n}}} m_{\mp}^i m_{\mp}^j \left[b_1^{\text{I}} \widehat{k_i} \widehat{k_j} \delta(z, \mathbf{k}) + 3b_{\text{NG}}^{\text{p}} \bar{A}_2 \left(\frac{k}{k_*} \right)^{\Delta_p} \hat{p}_i \hat{p}_j \phi(\mathbf{k}) \right] \quad (\text{B.1})$$

with $x \equiv k\chi(z)$ and $\hat{\mathbf{k}} \equiv \mathbf{k}/k$. In performing the expansion in terms of the spherical harmonics, we choose the z axis along the direction of $\hat{\mathbf{p}}$, i.e., $\hat{\mathbf{p}} = (0, 0, 1)$. With this choice, we obtain $m_{\pm}^i \hat{p}_i = -\sin\theta/\sqrt{2}$. For our purpose, we write the basis of the Fourier mode expansion as

$$e^{ix \hat{\mathbf{k}} \cdot \hat{\mathbf{n}}} = \sum_{l=0}^{\infty} (2l+1) i^l j_l(x) \mathcal{P}_l(\hat{\mathbf{k}} \cdot \hat{\mathbf{n}}) = 4\pi \sum_{l=0}^{\infty} \sum_{m=-l}^l i^l j_l(x) Y_{lm}(\hat{\mathbf{n}}) Y_{lm}^*(\hat{\mathbf{k}}). \quad (\text{B.2})$$

Using $\widehat{k_i} e^{ix \hat{\mathbf{k}} \cdot \hat{\mathbf{n}}} = (1/ix) \partial / \partial \hat{n}^i e^{ix \hat{\mathbf{k}} \cdot \hat{\mathbf{n}}}$ and

$$\pm_2 Y_{lm}(\hat{\mathbf{n}}) = 2 \sqrt{\frac{(l-2)!}{(l+2)!}} m_{\mp}^i m_{\mp}^j \frac{\partial^2}{\partial \hat{n}^i \partial \hat{n}^j} Y_{lm}(\hat{\mathbf{n}}),$$

we obtain the contribution from the first term as

$$a_{lm}^{(0)} = -b_1^{\text{I}} \sqrt{\frac{(l+2)!}{(l-2)!}} \int \frac{d^3 \mathbf{k}}{(2\pi)^{\frac{3}{2}}} \int dz \frac{dN_{\text{I}}}{dz} \frac{1}{x^2} i^l j_l(x) Y_{lm}^*(\hat{\mathbf{k}}) \delta(z, \mathbf{k}) \quad (\text{B.3})$$

for $l \geq 2$ and $a_{lm}^{(0)} = 0$ for $l = 0, 1$. Here, we inserted the redshift distribution of the galaxy sample dN_{I}/dz . Using Eq. (B.2), the contribution from the second term can be expressed as

$$a_{lm}^{(p)} = 2\pi \sqrt{\frac{(l-2)!}{(l+2)!}} \sum_{l'=0}^{\infty} \sum_{m'=-l'}^{l'} i^{l'} \int \frac{d^3 \mathbf{k}}{(2\pi)^{\frac{3}{2}}} \int dz \frac{dN_{\text{I}}}{dz} \phi(\mathbf{k}) j_{l'}(x) Y_{l'm'}(\hat{\mathbf{k}}) \\ \times \int d\Omega_{\mathbf{n}} Y_{lm}^*(\hat{\mathbf{n}}) \bar{\partial}^2 [Y_{l'm'}(\hat{\mathbf{n}}) \sin^2 \theta]. \quad (\text{B.4})$$

Since the constant vector $\hat{\boldsymbol{p}}$ violates the global rotation symmetry, $a_{lm}^{(p)}$ can be contaminated by non-diagonal multipoles with $l' \neq l$ and $m' \neq m$, while $a_{lm}^{(0)}$ does not depend on contributions of other multipoles. Performing the integral over the solid angle of $\hat{\boldsymbol{n}}$, which is lengthy but straightforward, we obtain Eq. (4.3), where coefficients $\alpha_{l,m}^{(s)}$ are given by

$$\alpha_{l,m}^{(0)} = -\frac{2(l-1)(l+2)\{l(l+1) - 3m^2\}}{(2l-1)(2l+3)} \quad (-l \leq m \leq l), \quad (\text{B.5})$$

$$\alpha_{l,m}^{(+1)} = -2m(l-1)\sqrt{\frac{(l-m+1)(l+m+1)}{(2l+1)(2l+3)}} \quad (l \geq 1, -l \leq m \leq l), \quad (\text{B.6})$$

$$\alpha_{l,m}^{(-1)} = 2m(l+2)\sqrt{\frac{(l-m)(l+m)}{(2l-1)(2l+1)}} \quad (-l+1 \leq m \leq l-1), \quad (\text{B.7})$$

$$\alpha_{l,m}^{(+2)} = \frac{l(l-1)\sqrt{(l-m+2)(l+m+2)(l+m+1)(l-m+1)}}{(2l+3)\sqrt{(2l+1)(2l+5)}} \quad (l \geq 2, -l \leq m \leq l), \quad (\text{B.8})$$

$$\alpha_{l,m}^{(-2)} = \frac{(l+1)(l+2)\sqrt{(l-m)(l+m)(l+m-1)(l-m-1)}}{(2l-1)\sqrt{(2l-3)(2l+1)}} \quad (-l+2 \leq m \leq l-2), \quad (\text{B.9})$$

and otherwise 0.

B.2 Rotation of axis

In the previous subsection, we calculated the angular power spectrum, choosing the z -axis (with $\theta = 0$) such that being along $\hat{\boldsymbol{p}}$. With this choice, we found that there is no cross-correlations between different ms . Next, we will show that the diagonalization over m is specific for this choice of the axis and in general there exist the cross-correlations.

Rotating the z axis to the direction (θ, ψ) changes the coefficients ${}_s a_{lm}$ of the expansion in terms of the spin weighted spherical harmonics ${}_s Y_{lm}$ as

$${}_s \tilde{a}_{lm} = \sqrt{\frac{4\pi}{2l+1}} (-1)^m \sum_{m'} {}_{-m} Y_{lm'}(\theta, \psi) {}_s a_{lm'}. \quad (\text{B.10})$$

Using this expression, we find that a_{lm}^{E} and a_{lm}^{B} both transform in the same way as

$$\tilde{a}_{lm}^X = \sqrt{\frac{4\pi}{2l+1}} (-1)^m \sum_{m'} {}_{-m} Y_{lm'}(\theta, \psi) a_{lm'}^X \quad (\text{B.11})$$

for $X = \text{E}, \text{B}$ and the angular power spectra in the two frames are related as

$$\begin{aligned} \langle \tilde{a}_{lm}^X \tilde{a}_{l'm'}^{Y*} \rangle &= (-1)^{m+m'} \sqrt{\frac{4\pi}{2l+1}} \sqrt{\frac{4\pi}{2l'+1}} \\ &\quad \times \sum_{\bar{m}} {}_{-m} Y_{l\bar{m}}(\theta, \psi) {}_{-m'} Y_{l'\bar{m}}^*(\theta, \psi) \langle a_{l\bar{m}}^X a_{l'\bar{m}}^{Y*} \rangle \end{aligned} \quad (\text{B.12})$$

for $X, Y = \text{E}, \text{B}$. Now, we see that in a general frame, both of l and m are not diagonal.

References

- [1] N. Arkani-Hamed and J. Maldacena, *Cosmological Collider Physics*, [1503.08043](#).
- [2] X. Chen and Y. Wang, *Large non-Gaussianities with Intermediate Shapes from Quasi-Single Field Inflation*, *Phys. Rev.* **D81** (2010) 063511 [[0909.0496](#)].
- [3] T. Noumi, M. Yamaguchi and D. Yokoyama, *Effective field theory approach to quasi-single field inflation and effects of heavy fields*, *JHEP* **06** (2013) 051 [[1211.1624](#)].
- [4] PLANCK collaboration, P. A. R. Ade et al., *Planck 2015 results. XVII. Constraints on primordial non-Gaussianity*, *Astron. Astrophys.* **594** (2016) A17 [[1502.01592](#)].
- [5] LSST SCIENCE, LSST PROJECT collaboration, P. A. Abell et al., *LSST Science Book, Version 2.0*, [0912.0201](#).
- [6] EUCLID collaboration, R. Laureijs et al., *Euclid Definition Study Report*, [1110.3193](#).
- [7] D. Spergel et al., *Wide-Field InfraRed Survey Telescope-Astrophysics Focused Telescope Assets WFIRST-AFTA Final Report*, [1305.5422](#).
- [8] N. Dalal, O. Dore, D. Huterer and A. Shirokov, *The imprints of primordial non-gaussianities on large-scale structure: scale dependent bias and abundance of virialized objects*, *Phys. Rev.* **D77** (2008) 123514 [[0710.4560](#)].
- [9] S. Matarrese and L. Verde, *The effect of primordial non-Gaussianity on halo bias*, *Astrophys. J.* **677** (2008) L77 [[0801.4826](#)].
- [10] A. Slosar, C. Hirata, U. Seljak, S. Ho and N. Padmanabhan, *Constraints on local primordial non-Gaussianity from large scale structure*, *JCAP* **0808** (2008) 031 [[0805.3580](#)].
- [11] V. Desjacques, D. Jeong and F. Schmidt, *Large-Scale Galaxy Bias*, *Phys. Rept.* **733** (2018) 1 [[1611.09787](#)].
- [12] M. Alvarez et al., *Testing Inflation with Large Scale Structure: Connecting Hopes with Reality*, [1412.4671](#).
- [13] F. Schmidt, N. E. Chisari and C. Dvorkin, *Imprint of inflation on galaxy shape correlations*, *JCAP* **1510** (2015) 032 [[1506.02671](#)].
- [14] C. M. Hirata, R. Mandelbaum, M. Ishak, U. Seljak, R. Nichol, K. A. Pimbblet et al., *Intrinsic galaxy alignments from the 2SLAQ and SDSS surveys: Luminosity and redshift scalings and implications for weak lensing surveys*, *Mon. Not. Roy. Astron. Soc.* **381** (2007) 1197 [[astro-ph/0701671](#)].
- [15] R. Mandelbaum et al., *The WiggleZ Dark Energy Survey: Direct constraints on blue galaxy intrinsic alignments at intermediate redshifts*, *Mon. Not. Roy. Astron. Soc.* **410** (2011) 844 [[0911.5347](#)].
- [16] C. Heymans et al., *CFHTLenS tomographic weak lensing cosmological parameter constraints: Mitigating the impact of intrinsic galaxy alignments*, *Mon. Not. Roy. Astron. Soc.* **432** (2013) 2433 [[1303.1808](#)].
- [17] S. Singh, R. Mandelbaum and S. More, *Intrinsic alignments of SDSS-III BOSS LOWZ sample galaxies*, *Mon. Not. Roy. Astron. Soc.* **450** (2015) 2195 [[1411.1755](#)].
- [18] P. McDonald and U. Seljak, *How to measure redshift-space distortions without sample variance*, *JCAP* **0910** (2009) 007 [[0810.0323](#)].
- [19] U. Seljak, *Extracting primordial non-gaussianity without cosmic variance*, *Phys. Rev. Lett.* **102** (2009) 021302 [[0807.1770](#)].
- [20] N. E. Chisari, C. Dvorkin, F. Schmidt and D. Spergel, *Multitracing Anisotropic Non-Gaussianity with Galaxy Shapes*, *Phys. Rev.* **D94** (2016) 123507 [[1607.05232](#)].

- [21] D. Yamauchi, S. Yokoyama and K. Takahashi, *Multitracer technique for galaxy bispectrum: An application to constraints on nonlocal primordial non-Gaussianities*, *Phys. Rev.* **D95** (2017) 063530 [[1611.03590](#)].
- [22] J. Gleyzes, R. de Putter, D. Green and O. Doré, *Biasing and the search for primordial non-Gaussianity beyond the local type*, *JCAP* **1704** (2017) 002 [[1612.06366](#)].
- [23] G. Cabass, E. Pajer and F. Schmidt, *Imprints of Oscillatory Bispectra on Galaxy Clustering*, [1804.07295](#).
- [24] S. Yokoyama and J. Soda, *Primordial statistical anisotropy generated at the end of inflation*, *JCAP* **0808** (2008) 005 [[0805.4265](#)].
- [25] N. Bartolo, E. Dimastrogiovanni, M. Liguori, S. Matarrese and A. Riotto, *An Estimator for statistical anisotropy from the CMB bispectrum*, *JCAP* **1201** (2012) 029 [[1107.4304](#)].
- [26] M. Takada and W. Hu, *Power Spectrum Super-Sample Covariance*, *Phys. Rev.* **D87** (2013) 123504 [[1302.6994](#)].
- [27] K. Akitsu, M. Takada and Y. Li, *Large-scale tidal effect on redshift-space power spectrum in a finite-volume survey*, *Phys. Rev.* **D95** (2017) 083522 [[1611.04723](#)].
- [28] PLANCK collaboration, P. A. R. Ade et al., *Planck 2015 results. XIII. Cosmological parameters*, *Astron. Astrophys.* **594** (2016) A13 [[1502.01589](#)].
- [29] A. Lewis, A. Challinor and A. Lasenby, *Efficient computation of CMB anisotropies in closed FRW models*, *Astrophys. J.* **538** (2000) 473 [[astro-ph/9911177](#)].
- [30] F. Schmidt and D. Jeong, *Cosmic Rulers*, *Phys. Rev.* **D86** (2012) 083527 [[1204.3625](#)].
- [31] P. Catelan, M. Kamionkowski and R. D. Blandford, *Intrinsic and extrinsic galaxy alignment*, *Mon. Not. Roy. Astron. Soc.* **320** (2001) L7 [[astro-ph/0005470](#)].
- [32] C. M. Hirata and U. Seljak, *Intrinsic alignment-lensing interference as a contaminant of cosmic shear*, *Phys. Rev.* **D70** (2004) 063526 [[astro-ph/0406275](#)].
- [33] M. A. Troxel and M. Ishak, *The Intrinsic Alignment of Galaxies and its Impact on Weak Gravitational Lensing in an Era of Precision Cosmology*, *Phys. Rept.* **558** (2014) 1 [[1407.6990](#)].
- [34] B. Joachimi et al., *Galaxy alignments: An overview*, *Space Sci. Rev.* **193** (2015) 1 [[1504.05456](#)].
- [35] D. Baumann and L. McAllister, *Inflation and String Theory*, Cambridge Monographs on Mathematical Physics. Cambridge University Press, 2015, [10.1017/CBO9781316105733](#), [[1404.2601](#)].
- [36] S. Deser and A. Waldron, *Arbitrary spin representations in de Sitter from dS / CFT with applications to dS supergravity*, *Nucl. Phys.* **B662** (2003) 379 [[hep-th/0301068](#)].
- [37] H. Lee, D. Baumann and G. L. Pimentel, *Non-Gaussianity as a Particle Detector*, *JHEP* **12** (2016) 040 [[1607.03735](#)].
- [38] T. Tanaka and Y. Urakawa, *Conservation of ζ with radiative corrections from heavy field*, *JCAP* **1606** (2016) 020 [[1510.05059](#)].
- [39] T. Tanaka and Y. Urakawa, *Large gauge transformation, Soft theorem, and Infrared divergence in inflationary spacetime*, *JHEP* **10** (2017) 127 [[1707.05485](#)].
- [40] S. Weinberg, *Adiabatic modes in cosmology*, *Phys. Rev.* **D67** (2003) 123504 [[astro-ph/0302326](#)].
- [41] S. Endlich, A. Nicolis and J. Wang, *Solid Inflation*, *JCAP* **1310** (2013) 011 [[1210.0569](#)].
- [42] PLANCK collaboration, P. A. R. Ade et al., *Planck 2015 results. XX. Constraints on inflation*, *Astron. Astrophys.* **594** (2016) A20 [[1502.02114](#)].

- [43] J. Kim and E. Komatsu, *Limits on anisotropic inflation from the Planck data*, *Phys. Rev.* **D88** (2013) 101301 [[1310.1605](#)].
- [44] M. Shiraishi, N. S. Sugiyama and T. Okumura, *Polypolar spherical harmonic decomposition of galaxy correlators in redshift space: Toward testing cosmic rotational symmetry*, *Phys. Rev.* **D95** (2017) 063508 [[1612.02645](#)].
- [45] N. S. Sugiyama, M. Shiraishi and T. Okumura, *Limits on statistical anisotropy from BOSS DR12 galaxies using bipolar spherical harmonics*, *Mon. Not. Roy. Astron. Soc.* **473** (2018) 2737 [[1704.02868](#)].
- [46] N. Bartolo, A. Kehagias, M. Liguori, A. Riotto, M. Shiraishi and V. Tansella, *Detecting higher spin fields through statistical anisotropy in the CMB and galaxy power spectra*, *Phys. Rev.* **D97** (2018) 023503 [[1709.05695](#)].
- [47] A. Kehagias and A. Riotto, *On the Inflationary Perturbations of Massive Higher-Spin Fields*, *JCAP* **1707** (2017) 046 [[1705.05834](#)].
- [48] G. Franciolini, A. Kehagias and A. Riotto, *Imprints of Spinning Particles on Primordial Cosmological Perturbations*, *JCAP* **1802** (2018) 023 [[1712.06626](#)].
- [49] J. Blazek, N. MacCrann, M. A. Troxel and X. Fang, *Beyond linear galaxy alignments*, [1708.09247](#).
- [50] A. Moradinezhad Dizgah and C. Dvorkin, *Scale-Dependent Galaxy Bias from Massive Particles with Spin during Inflation*, *JCAP* **1801** (2018) 010 [[1708.06473](#)].
- [51] C. Chang, M. Jarvis, B. Jain, S. M. Kahn, D. Kirkby, A. Connolly et al., *The Effective Number Density of Galaxies for Weak Lensing Measurements in the LSST Project*, *Mon. Not. Roy. Astron. Soc.* **434** (2013) 2121 [[1305.0793](#)].
- [52] D. N. Limber, *The Analysis of Counts of the Extragalactic Nebulae in Terms of a Fluctuating Density Field. II*, *Astrophys. J.* **119** (1954) 655.
- [53] M. LoVerde and N. Afshordi, *Extended Limber Approximation*, *Phys. Rev.* **D78** (2008) 123506 [[0809.5112](#)].
- [54] F. Schmidt and M. Kamionkowski, *Halo Clustering with Non-Local Non-Gaussianity*, *Phys. Rev.* **D82** (2010) 103002 [[1008.0638](#)].
- [55] T. Matsubara, *Deriving an Accurate Formula of Scale-dependent Bias with Primordial Non-Gaussianity: An Application of the Integrated Perturbation Theory*, *Phys. Rev.* **D86** (2012) 063518 [[1206.0562](#)].
- [56] J. Blazek, Z. Vlah and U. Seljak, *Tidal alignment of galaxies*, *JCAP* **1508** (2015) 015 [[1504.02510](#)].
- [57] E. Sefusatti, J. R. Fergusson, X. Chen and E. P. S. Shellard, *Effects and Detectability of Quasi-Single Field Inflation in the Large-Scale Structure and Cosmic Microwave Background*, *JCAP* **1208** (2012) 033 [[1204.6318](#)].
- [58] K. Kogai et al., in preparation, .
- [59] M. Tegmark, A. Taylor and A. Heavens, *Karhunen-Loeve eigenvalue problems in cosmology: How should we tackle large data sets?*, *Astrophys. J.* **480** (1997) 22 [[astro-ph/9603021](#)].
- [60] D. Scott, D. Contreras, A. Narimani and Y.-Z. Ma, *The information content of cosmic microwave background anisotropies*, *JCAP* **1606** (2016) 046 [[1603.03550](#)].
- [61] L. Verde, *Statistical methods in cosmology*, *Lect. Notes Phys.* **800** (2010) 147 [[0911.3105](#)].
- [62] T. Tanaka and Y. Urakawa, *Dominance of gauge artifact in the consistency relation for the primordial bispectrum*, *JCAP* **1105** (2011) 014 [[1103.1251](#)].

- [63] E. Pajer, F. Schmidt and M. Zaldarriaga, *The Observed Squeezed Limit of Cosmological Three-Point Functions*, *Phys. Rev.* **D88** (2013) 083502 [[1305.0824](#)].
- [64] D. Alonso, P. Bull, P. G. Ferreira, R. Maartens and M. Santos, *Ultra large-scale cosmology in next-generation experiments with single tracers*, *Astrophys. J.* **814** (2015) 145 [[1505.07596](#)].
- [65] A. Moradinezhad Dizgah, H. Lee, J. B. Muñoz and C. Dvorkin, *Galaxy Bispectrum from Massive Spinning Particles*, *JCAP* **1805** (2018) 013 [[1801.07265](#)].
- [66] F. Schmidt and D. Jeong, *Large-Scale Structure with Gravitational Waves II: Shear*, *Phys. Rev.* **D86** (2012) 083513 [[1205.1514](#)].
- [67] F. Schmidt, E. Pajer and M. Zaldarriaga, *Large-Scale Structure and Gravitational Waves III: Tidal Effects*, *Phys. Rev.* **D89** (2014) 083507 [[1312.5616](#)].
- [68] S. Saga, D. Yamauchi and K. Ichiki, *Weak lensing induced by second-order vector mode*, *Phys. Rev.* **D92** (2015) 063533 [[1505.02774](#)].
- [69] E. Castorina, Y. Feng, U. Seljak and F. Villaescusa-Navarro, *Primordial non-Gaussianities and zero bias tracers of the Large Scale Structure*, [1803.11539](#).